



# Depth structure of Ningaloo Niño/Niña events and associated drivers

Svenja Ryan\*, Caroline C. Ummenhofer, Glen Gawarkiewicz

*Woods Hole Oceanographic Institution, Woods Hole, Massachusetts, USA*

Patrick Wagner, Markus Scheinert, Arne Biastoch, Claus W. Böning

*GEOMAR, Helmholtz Centre for Ocean Research Kiel, Kiel, Germany*

\*Corresponding author address: Physical Oceanography, Woods Hole Oceanographic Institution,

266 Woods Hole Road, Woods Hole, Massachusetts/USA.

E-mail: sryan@whoi.edu

Generated using v4.3.2 of the AMS L<sup>A</sup>T<sub>E</sub>X template

1

**Early Online Release:** This preliminary version has been accepted for publication in *Journal of Climate*, may be fully cited, and has been assigned DOI 10.1175/JCLI-D-19-1020.1. The final typeset copyedited article will replace the EOR at the above DOI when it is published.

## ABSTRACT

9 Marine heatwaves along the coast of Western Australia, referred to as Ninga-  
10 loo Niño, have had dramatic impacts on the ecosystem in the recent decade.  
11 A number of local and remote forcing mechanisms have been put forward,  
12 however little is known about the depth structure of such temperature ex-  
13 tremes. Utilizing an eddy-active global Ocean General Circulation Model,  
14 Ningaloo Niño and the corresponding cold Ningaloo Niña events are inves-  
15 tigated between 1958-2016, with focus on their depth structure. The rela-  
16 tive roles of buoyancy and wind forcing are inferred from sensitivity experi-  
17 ments. Composites reveal a strong symmetry between cold and warm events  
18 in their vertical structure and associated large-scale spatial patterns. Tempera-  
19 ture anomalies are largest at the surface, where buoyancy forcing is dominant  
20 and extend down to 300m depth (or deeper), with wind forcing being the main  
21 driver. Large-scale subsurface anomalies arise from a vertical modulation of  
22 the thermocline, extending from the western Pacific into the tropical eastern  
23 Indian Ocean. The strongest Ningaloo Niños in 2000 and 2011 are unprece-  
24 dented compound events, where long-lasting high temperatures are accom-  
25 panied by extreme freshening, which emerges in association with La Niñas,  
26 more common and persistent during the negative phase of the Interdecadal  
27 Pacific Oscillation. It is shown that Ningaloo Niños during La Niña phases  
28 have a distinctively deeper reach and are associated with a strengthening of  
29 the Leeuwin Current, while events during El Niño are limited to the surface  
30 layer temperatures, likely driven by local atmosphere-ocean feedbacks, with-  
31 out a clear imprint on salinity and velocity.

## 1. Introduction

Marine Heatwaves (MHWs) are extreme events characterized by extended periods of anomalously warm ocean temperatures and can have drastic ecological and socioeconomical impacts. They can lead to mass mortality of marine organisms (Mills et al. 2013; Short et al. 2015; Jones et al. 2018), coral bleaching (Benthuisen et al. 2018) and can alter structures of regional marine ecosystems (Wernberg et al. 2013, 2016; Smale et al. 2019). Furthermore, MHWs often impact fisheries adversely affecting a region's economy (Mills et al. 2013). In the face of globally warming temperatures and enhanced greenhouse gas emissions, an increase in intensity, frequency, and duration of MHWs has been observed (Frölicher and Laufkötter 2018; Oliver et al. 2018). In this study we explore the depth structure of these extreme events on the southeast Indian Ocean and associated signals in salinity in addition to temperature.

One of the strongest observed MHWs occurred off the coast of Western Australia (WA) in austral summer of 2010/2011, where maximum temperature anomalies of over 3°C were reached in February 2011. This event led to the first recorded coral bleaching event at the World Heritage Ningaloo Reef and extensive loss of kelp forest associated with a regime shift from subtropical to tropical species along the western Australian coast (Wernberg et al. 2013, 2016; Pearce and Feng 2013). The interannual variability of sea surface temperatures (SST) in this region has been dubbed Ningaloo Niño, in analogy to interannual warming events in other eastern boundary systems such as El Niño and Benguela Niño (Feng et al. 2013).

The 2011 MHW was associated with the strongest recorded transports of the poleward flowing Leeuwin Current (LC, see Fig. 1) during summer along the WA coast, which resulted in an increased southward heat and freshwater transport. The surge of the LC has been attributed to the presence of strong La Niña conditions in 2010/2011 (Feng et al. 2013). Here, sea surface height



55 (SSH) anomalies created by anomalous easterly winds in the western Pacific propagate through  
56 the Indonesian Seas following a coastal waveguide (Clarke and Liu 1994; Wijffels et al. 2004) ul-  
57 timately reaching the Australian continent and strengthening the LC. Warm surface temperatures  
58 were then amplified by local air-sea interaction via the wind-evaporation-SST (WES) feedback,  
59 also leading to increased rainfall over the Australian continent (Feng et al. 2013; Kataoka et al.  
60 2014; Benthuisen et al. 2014; Marshall et al. 2015).

61 While key processes driving the 2011 event, and the general variability associated with Ningaloo  
62 Niño and Niña (the cold equivalent) have been put forward, little is known about the depth structure  
63 of these extreme events. Using a regional ocean model Benthuisen et al. (2014) performed a  
64 temperature budget over the upper 60m and showed that the warming in 2011 can be attributed  
65 approximately 2/3 to oceanic advection of warmer, tropical water by the LC and 1/3 to positive air-  
66 sea heat flux. Furthermore, Kataoka et al. (2017) showed that mixed layer variability is important  
67 for the amplification of surface temperatures as it changes the sensitivity to surface fluxes: i.e. a  
68 shallow mixed layer will heat up more quickly compared to a deep mixed layer. However, to the  
69 best of our knowledge, no study has investigated the depth structure beyond the surface mixed  
70 layer. For the 2011 event, sporadic observations suggested that temperature anomalies are surface  
71 intensified (Benthuisen et al. 2014), nevertheless anomalies at greater depth can have important  
72 implications. Domingues et al. (2006) showed that the LC loses most of its heat to the interior  
73 Indian Ocean during its southward progression. They found that the offshore heat transfer via  
74 eddy-fluxes accounts for about 70% of the warming of a large area in the southeastern Indian  
75 Ocean. Furthermore, anomalies with greater vertical scales, exceeding the winter mixed layer  
76 depth, may have the potential to persist longer as they are then insulated from surface processes  
77 and depending on the regional circulation could be subject to reemergence.

78 Salinity has a significant influence on the ocean stratification and circulation in the southeastern  
79 Indian Ocean (e.g. Feng et al. 2015; Hu et al. 2019) and is therefore essential for the analysis of  
80 extreme event drivers and ultimately predictions. Feng et al. (2015) showed that excessive precip-  
81 itation in the Maritime Continent leads to a strong freshening of surface waters which then were  
82 advected westward and entrained into the LC, contributing about 30% to its observed strength-  
83 ening. Furthermore, local precipitation anomalies can occur when the WES feedback is active  
84 during the initiation phase of Ningaloo Niño (Kataoka et al. 2014; Marshall et al. 2015). Due  
85 to the sparseness of salinity observations, the depth extent of these fresh anomalies has not been  
86 explored in a multi-event or composite study in the Ningaloo region.

87 To address both the vertical structure of temperature and salinity associated with MHWs, three-  
88 dimensional ocean models can serve as valuable tools as already demonstrated by Benthuisen  
89 et al. (2014), (Oliver et al. 2017) and Behrens et al. (2019). Additionally, global models allow the  
90 analysis of the impacts of large-scale climate modes onto the regional circulation and subsurface  
91 signals. While, reanalysis products also represent a great resource, they are by design not energy  
92 and mass conserving, which poses some limitations to the analysis of physical processes. Ocean  
93 general circulation models may have certain biases, however, obey the equations of motion and  
94 conservation laws.

95 In this study we utilize output of an eddy-active ( $1/4^\circ$ ) global ocean general circulation model  
96 to investigate temporal and spatial characteristics of Ningaloo Niño/Niña with a focus on the ver-  
97 tical structure of extreme events across the upper 800m, and assess the relative role of wind and  
98 buoyancy (thermohaline) forcing using sensitivity experiments. We are building on previously  
99 proposed mechanisms and set these into context by presenting subsurface signals. The paper is  
100 structured as follows: In section 2 we give a short overview of the oceanographic and geographical  
101 setting of the study region. Data and methods are presented in section 3, including a model descrip-

tion and validation followed by the approach taken for the extreme event detection. The general temporal variability at the surface associated with Ningaloo Niño/Niña is elaborated in section 4, while spatial and vertical structures of extreme event composites are addressed in section 5. In the following, the 2010/2011 Ningaloo Niño event is used as a case study in section 6. The paper concludes by putting the results into context with large-scale climate variability in section 7 and ends with a short discussion, concluding remarks and a summarizing schematic in section 8.

## 2. Oceanographic and geographical setting

The southeastern Indian Ocean features unique geographical and oceanographic settings (Fig. 1). A low-latitude connection from the Pacific to the Indian Ocean via the Indonesian Archipelago allows the transfer of very warm waters from the western Pacific into the eastern Indian Ocean, which are freshened and mixed in the shallow Indonesian Seas, forming a unique warm and fresh water mass (Gordon 2005). It is then transported westward across the Indian Ocean by the South Equatorial Current and poleward via the LC. The Indonesian Throughflow (ITF) plays a major role for the global thermohaline circulation (Sprintall et al. 2014) with an approximate transport of 15 Sv (Gordon et al. 2010) and has strong impacts on the regional hydrography. The warm and fresh ITF waters are much lighter than those found in the southeastern Indian Ocean, which creates a meridional pressure gradient, that drives surface eastward flow forming the South Indian Countercurrent (Menezes et al. 2014, see Fig. 1a). This surface flow feeds into the LC along the western coast of Australia, which is the only poleward flowing eastern boundary current in the global ocean (Smith et al. 1991) persisting despite prevailing southeasterly trade winds. The LC is additionally sourced from ITF waters via the salinity-driven East Gyral Current (Domingues et al. 2007; Menezes et al. 2013, 2014), which recirculates parts of the westward-flowing ITF waters, while small direct routes exist along the continental slope of northwestern Australia (Fig. 1a).

125 Hence, the LC transports warm and fresh waters southward along the coast, which creates a zonal  
126 density gradient in the presence of saltier waters offshore, which in turn creates a geostrophic  
127 contribution to the southward flow.

128 The LC is located over the continental slope and extends roughly over the upper 200m of the  
129 water column (Fig. 1c and d). Its mean transport approximates to 3.4Sv with weakest transport in  
130 austral summer and strongest transport in austral winter (Feng et al. 2003). While the seasonality  
131 is confirmed by several studies, Furue et al. (2017) found smaller mean LC transports by focus-  
132 ing on a narrower band along the coast ( $0.7^\circ$  longitude from coast), whereas Feng et al. (2003)  
133 estimated their transport between  $110^\circ\text{E}$  and the coast. Slightly offshore hugging the continental  
134 slope between 200-600m, the Leeuwin Undercurrent (LUC) flows equatorward (Fig. 1c and d)  
135 with an estimated mean transport of about 5 Sv based on current meter measurements (Smith et al.  
136 1991), however, its dynamics are not clear.

137 The ITF is driven by a large-scale pressure gradient between the western Pacific and the eastern  
138 Indian Ocean and its variability has been mainly attributed to El Niño - Southern Oscillation  
139 (ENSO Hu and Sprintall 2016). However, other modes of variability on various timescales, such  
140 as the Indian Monsoon, the Indian Ocean Dipole or the Interdecadal Pacific Oscillation (IPO)  
141 have impacts as well, making the eastern Indian Ocean a very complex ocean-atmosphere coupled  
142 system.

### 143 **3. Data and methods**

#### 144 *a. Datasets*

145 High-resolution ( $1/4^\circ$ ) global, daily SSTs from the Advanced Very High Resolution Radiometer  
146 (AVHRR) satellite data product (NOAA OISST V2, Reynolds et al. 2007) and the  $1^\circ \times 1^\circ$ , monthly

Hadley Centre Sea Ice and Sea Surface Temperature (HadISST) product (Rayner et al. 2003) are used as observational products of SST. We use gridded salinity fields from the in situ analysis system (ISAS-15) tool, which is compiled from Argo float profiles and is available from 2002-2015 (Fabienne 2012). We chose this dataset over other reanalysis products that date further back because reliable coherent salinity measurements have only become available with Argo since 2000. Interannual and decadal variability is analyzed in the context of the IPO and the Oceanic Nino Index (ONI). The IPO represents a distinct mode of climate variability and is expressed as the IPO Tripole Index (TPI, Henley et al. 2015), which is associated with a distinct ‘tripole’ pattern of SST anomalies in the Pacific, with three large centers of action and variations on decadal timescales. The ONI represents the 3 month running mean of SST anomalies (ERSST.v5) in the Niño 3.4 region ( $5^{\circ}\text{N} - 5^{\circ}\text{S}, 120^{\circ} - 170^{\circ}\text{W}$ ). El Niño and La Niña events are characterized by an index value above 0.5 or below -0.5, respectively. Daily remotely sensed, delayed-time (reprocessed) absolute dynamic height data at  $0.25^{\circ}$  spatial resolution is used for model validation. It is provided by the E.U. Copernicus Marine Monitoring Service (CMEMS, formerly distributed by Archiving, Validation and Interpretation of Satellite Oceanographic data (AVISO)). Monthly tide gauge sea level data at Fremantle, Western Australia (Station ID: 111) is obtained from the Permanent Service For Mean Sea Level, covering the time period 1897-2019.

#### *b. Model description and experiments*

We use a global ocean model configuration of the Nucleus for European Modeling of the Ocean (NEMO) code, version 3.6 (Madec 2016) with a global tripolar ORCA grid at  $1/4^{\circ}$  horizontal resolution. The vertical grid consists of 46 z levels with varying layer thickness from 6 m at the surface to 250 m in the deepest levels. Bottom topography is interpolated from 2-Minute Gridded Global Relief Data ETOPO2v2 and represented by partial steps (Barnier et al. 2006). The

170 ocean model is coupled to the Louvain-La-Neuve sea-ice Model version 2 (LIM2-VP, Fichefet and  
171 Maqueda 1997).

172 The model is forced with the JRA55-do forcing (Tsujino et al. 2018) which builds on the JRA55  
173 atmospheric reanalysis product but is adjusted to match observational datasets. Bulk formulas  
174 from Large and Yeager (2009) are used to calculate surface fluxes. A relaxation of sea surface  
175 salinity (SSS) towards observed climatological conditions (World Ocean Database, Levitus et al.  
176 1998) is applied, a method commonly used in global ocean models to prevent spurious model drift  
177 (Griffies et al. 2009). The choice of a very long damping time scale (corresponding to 1 yr for a  
178 50 m surface layer) limits damping of intraseasonal anomaly signals.

179 All experiments used in this study are started from a 30-year-long spin-up integration (1980-  
180 2009), which was initialized with hydrography from the World Ocean Database (Levitus et al.  
181 1998) with modifications in the polar regions from PHC (Polar science center Hydrographic Cli-  
182 matology), which represents a global ocean hydrography with a high-quality Arctic Ocean (Steele  
183 et al. 2001). The spin-up started from an ocean at rest and was driven by interannually varying  
184 atmospheric boundary conditions (JRA55-do forcing). After this, all simulations were integrated  
185 from 1958 to 2016 and monthly output fields are analyzed.

186 Three different simulations are used in this study. The hindcast experiment (*hindcast*) is forced  
187 with interannually varying atmospheric boundary conditions. In addition, two sensitivity exper-  
188 iments were conducted with the aim to separate impacts of wind and buoyancy (i.e. heat and  
189 freshwater fluxes) forcing. For these, interannual variability in the forcing was restricted to either  
190 the buoyancy (*buoyancy*) or momentum fluxes (*wind*) respectively, while the same seasonal cycle  
191 was repeated each year for the other component. It should be noted that the experiments cannot  
192 eliminate the role of e.g. wind forcing in driving buoyancy fluxes and vice versa buoyancy fluxes  
193 that may drive changes in atmospheric circulation, thus in the wind.

194 No climatological normal year forcing, as described in Large and Yeager (2009) for the CORE  
195 experiments (Coordinated Ocean-ice Reference Experiments), is available for the JRA55-do  
196 dataset. Thus a “Repeated Year Forcing” (RYF) similar to Stewart et al. (2020) was constructed.  
197 In the RYF approach, carefully selected years from the forcing dataset are used repeatedly to elim-  
198 inate interannual variations from the forcing. Based on a range of climate indices Stewart et al.  
199 (2020) identified years that are characterized by neutral phases of these indices. Based on these,  
200 we chose the period from May 1990 to April 1991 to replace either the interannually varying  
201 momentum or buoyancy fluxes in our sensitivity experiments.

202 The analysis of ocean models forced by bulk formulations of air-sea heat fluxes has to account  
203 for the fact that the simulated SST is to some degree constrained by the prescribed atmospheric  
204 temperatures of the forcing dataset. We therefore limit our analysis to the subsurface layer, where  
205 the ocean is allowed to evolve more freely, i.e. exclude the top-layer ( $\sim 3$  m). Since our emphasis  
206 is on the subsurface (vertical) structure of the temperature and salinity fields, the results shown are  
207 not impacted by this choice. Furthermore, the mean difference over the whole integration between  
208 the first and second layer in the Ningaloo Niño region is low at  $0.04^{\circ}\text{C}$ , with a maximum of  $0.23^{\circ}\text{C}$   
209 over a very short period. For simplicity, we will refer to the second layer ( $\sim 9$  m) as the surface  
210 layer throughout the manuscript.

### 211 *c. Validation: Large-scale*

212 The model performance is validated by a comparison of the modeled sea level anomaly and  
213 associated variance with the AVISO satellite product. SSH is an important quantity in the Indo-  
214 Pacific region as indicator of ITF strength, signal propagation through the Indonesian Archipelago,  
215 ocean heat content, as well as the LC strength. A previous version of the model with a different

216 forcing has been used by Feng et al. (2008) to investigate the seasonal and interannual variability  
217 of the LC.

218 The model successfully reproduces the observed SSH gradients and patterns of associated vari-  
219 ance in the study region (Fig. 2). However, it underestimates the variance in the southeastern  
220 Indian Ocean (also found by Feng et al. 2008). The elevated variance can be attributed to Rossby  
221 waves that propagate westward from the eastern boundary. It is likely that the spatial resolution of  
222 the model is not sufficient to fully resolve this process.

223 The modeled mean ITF transport, defined as the maximum of the barotropic streamfunction be-  
224 tween 8-22°S along 114°E, is 14.5 Sv and thus agrees well with observational estimates of about  
225 15 Sv measured during the International Nusantara STRatification ANd Transport (INSTANT) pro-  
226 gram between 2004-2006 (Sprintall et al. 2009; Gordon et al. 2010). Furthermore, the model  
227 reproduces maximum velocities within the thermocline at around 100m depth within the Makas-  
228 sar Strait, as found by Gruenburg and Gordon (2018) from moored measurements.

229 The correlation between monthly observed sea level at Fremantle and the modeled sea level  
230 anomaly for the whole period of the integration is 0.82 ( $p < 0.01$ ). Following Feng et al. (2008),  
231 we derive the volume transport of the LC and LUC at 32°S between 110°E. Based on the mean  
232 vertical structure of velocities at this section we chose the upper 14 levels (3-191 m) to derive the  
233 LC. The mean modeled LC transport is 1.5 Sv which is noticeably lower than the observation-  
234 based estimate of 3.4 Sv by Feng et al. (2003). However, the seasonal cycle is represented well  
235 with maximum transport (2.8 Sv) in June and minimum transport during austral summer. Discrep-  
236 ancies between the modeled and observed transports may arise from differences in the forcings,  
237 in particular the meridional wind. Furthermore, Furue et al. (2017) obtain lower LC transport val-  
238 ues when focusing on a narrower band along the coast. Thus, differences in the offshore velocity  
239 structure in the model could also contribute to lower transports in our model. We conclude that



the high correlation of sea level anomalies together with the correct phasing of the seasonal cycle suggests that the model is suitable for our analysis.

#### *d. Extreme event detection and validation*

A common framework for MHW detection has been developed in recent years (Hobday et al. 2016, 2018), which allows a comparison of MHW metrics across different regions and seasons. The definition is based on daily SST data but was modified here to use monthly output fields from the global ocean simulations. The adapted approach employed the Ningaloo Niño Index (NNI), which has been used previously to study MHWs off the coast of WA (Kataoka et al. 2014, 2017, 2018; Marshall et al. 2015; Feng et al. 2015; Feng and Shinoda 2019). We adapt the NNI definition by Marshall et al. (2015), who use the average SST anomalies over the box region 110°E - 116°E, 22 – 32°S. The mean seasonal cycle is removed and anomalies are derived with respect to the full time period (1958-2016) as baseline.

Although the public interest in MHWs is increasing rapidly due to strong ecological and economic impacts, we also chose to include the analog cold extremes (Ningaloo Niña), which we will refer to as Marine Cold Spells (MCS) throughout the manuscript. Identifying similarities and differences between MHWs and MCSs may provide additional information about forcing mechanisms. Following the Hobday et al. (2016) definition, we define extreme events by the 90th and 10th percentile of the NNI temperature anomalies for MHWs and MCSs, respectively. Previous studies have focused on the December-January-February (DJF) properties of the NNI, when the largest temperature anomalies and variance are found, and detected extreme events based on standard deviation (Kataoka et al. 2014; Marshall et al. 2015). In the sense of the common MHW definition by Hobday et al. (2016), we derive a monthly threshold and thus allow the detection of events during the whole year. We detect 29 MHW and 34 MCS events (see Tables 1 & A1), with

about 1/3 occurring in austral summer (DJF). However, one MHW lasting from October 2010 to May 2012 has been manually separated into two events. All but two summer events detected by our definition (1958/1959, 1963/1964) were also detected by Marshall et al. (2015) and/or Kataoka et al. (2014) (see bold events in tables), indicating that the model and detection algorithm are performing well. Small differences are to be expected due to the different datasets, their spatial and temporal resolutions as well as different baselines. The MHW detection was also performed on the surface model layer, which we chose to exclude as described above, and the same events (including duration) were detected.

By applying an empirical orthogonal function (EOF) analysis for SST, Kataoka et al. (2014) and Marshall et al. (2015) showed that the NNI reflects the dominant mode of variability in observed SST fields over the region 100 – 120°E, 14 – 36°S. The EOF spatial pattern and principal component (PC) are derived for the HadISST dataset and compared to those of the surface temperature of the model output (Fig. 3a,b,d). The model reproduces the observed spatial patterns and we find good agreement between the PCs of the leading mode in observations and model ( $r = 0.83$ ,  $p < 0.01$ ). Furthermore, the modeled temperature NNI correlates well with the PCs, with  $r = 0.85$  ( $p < 0.01$ ) for the model PC and  $r = 0.67$  ( $p < 0.01$ ) for HadISST. The overall correlation between the modeled and observed temperature NNI is 0.96 ( $p < 0.01$ ).

We expand the analysis by defining the NNI index also for salinity. The EOF spatial pattern exhibits a slightly different spatial structure compared to temperature with maximum anomalies along the coast of Northwestern Australia which extend southward along the coast into the NNI box. The salinity NNI nevertheless captures the variability associated with the leading mode well, indicating the advective nature of these coastal signals due to the LC (Fig. 3e).

#### 285 *e. Statistics*

286 Monte-Carlo simulations are performed to test the significance of NNI vertical profiles for MHW  
287 and MCS composites. In total we detect 29 MHW events, which encompass 72 months. For the  
288 simulation, we randomly select 29 points in time, representing the individual events, and average  
289 the NNI properties in order to mimic the composites. To account for the possible auto-correlation  
290 associated with the events, we assume a mean duration of 2 months, i.e. for each random point in  
291 time, two consecutive months are taken into account for the composite. This procedure is repeated  
292  $10^5$  times, which produces a distribution of the respective variable at each depth level. The 5th  
293 and 95th percentile of that distribution are chosen as our significance level. This analysis thus  
294 indicates how significant the extreme event composites are in comparison to randomly occurring  
295 anomalies.

#### 296 **4. Ningaloo Niño variability**

297 The temperature and salinity NNI depicts strong interannual variability (Fig. 4a). A comparison  
298 with the NNI derived from monthly OISST data shows good agreement (anomalies:  $r = 0.9$ ,  $p <$   
299  $0.01$ , full:  $r = 0.98$ ,  $p < 0.01$ ), although there is a tendency for slightly lower amplitudes in the  
300 model. Salinity generally shows lower frequency variability than temperature, which suggests that  
301 the variability in both fields might be partly driven by different underlying processes. MHWs and  
302 MCSs are detected throughout the whole time period and warm anomalies are generally associated  
303 with fresh anomalies and vice versa (see Tables 1 & A1).

304 The largest MHWs in 1999/2000 and 2010/2011 are both associated with strong fresh anomalies  
305 of up to 0.4psu (Table 1) in the model. An average freshening of 0.2psu between 1999 and  
306 2002 has been described by Phillips et al. (2005) based on Argo float data and Feng et al. (2015)  
307 observed an anomaly of 0.3psu for the 2010/2011 event. Both these recent freshening events

308 as well as the one in the mid-1970s in the model NNI time series are captured by long-term  
309 observational data at Rottneest Island and were associated with extended periods of La Niña phases  
310 (Feng et al. 2015). The model also shows a freshening in the first half of the 1960s (no data is  
311 available at Rottneest during this time). Both events prior to 1980 are associated with heatwaves as  
312 well, which are of shorter duration (1-2 months), however, the intensity, i.e. maximum temperature  
313 anomaly, of the 1962 event is even slightly higher than the one of the 1999/2000 MHW (Table 1).  
314 The salinity NNI derived from the ISAS-15 gridded Argo dataset shows a fresh anomaly of 0.2 psu  
315 associated with the 2010/2011 Ningaloo Niño, i.e. is on the same order as the 2000 event. The  
316 comparison with observations suggests that the model captures the interannual variability in both  
317 temperature and salinity well, although the magnitude of the fresh anomalies might be slightly  
318 overestimated by the model. Nevertheless, this does not dismiss the general distinctness of these  
319 fresh anomalies and their co-occurrence with MHWs.

320 Similarly, persistent positive anomalies in salinity are associated with more frequent MCSs,  
321 with distinct events ( $\Delta S \approx 0.2$ ) in the first half of the 1990s and the mid-2000s, and two shorter  
322 but strong events in 2010 and 2016. Again the variability agrees well with the observations.

## 323 5. Extreme event composites

### 324 a. Depth structure

325 To investigate the depth structure of the detected MHWs and MCSs, composites of the mean  
326 vertical profile in the NNI box are derived (Fig. 5) for *hindcast* and both sensitivity experiments  
327 (*buoyancy*, *wind*). The same analysis but limited to the narrower LC band has been performed  
328 (Fig. B1). We adapted the definition by Furue et al. (2017) for the LC width, which used the  
329 200m isobath as the eastern boundary. The western boundary is marked by the location of the

eastern boundary minus  $0.7^\circ$  longitude (see red band in Fig. 1). A strong symmetry between warm and cold events is revealed across depth for temperature, salinity and meridional velocity in all three simulations. The largest anomalies are found at the surface for all variables in *hindcast*. Statistically significant (i.e. exceeding the gray shading in Fig. 5) temperature anomalies extend beyond the generally thin surface mixed layer down to 300m for MHWs and even deeper to 500m for MCSs, while non-significant anomalies with the respective sign are found up to a depth of 700m. Within the LC the anomalies are also significant at greater depth (Fig. B1). Feng et al. (2015) find positive anomalies down to 300m close to the coast for the 2011 event using Bluelink ReANalysis, which is a data-assimilating hydrodynamic model product. Thus, our model seems to produce realistic vertical structures.

The sensitivity experiments suggest that for both, cold and warm extremes, thermohaline forcing (*buoyancy*) is the largest contributor to the surface anomalies (approx.  $2/3$  over  $1/3$ ). Velocity anomalies in *buoyancy* (Fig 5c) are not significant. Thus heat and freshwater fluxes seem to have an overall weak impact on the LC strength in the composites, while this can, of course, be different for individual events. Temperature anomalies in *buoyancy* become non-significant below about 150m and are close to zero below 200m depth.

Experiment *wind* depicts a subsurface maximum of temperature anomalies at roughly 100 – 150m depth and is generally responsible for the depth extent of the events. Maximum temperature anomalies are found at the depth of the thermocline, i.e. where a strong vertical temperature gradient exists, and composites of the in-situ profiles (not shown) reveal shoaled isotherms during MHWs and deepened isotherms during MCSs. This subsurface maximum is again more pronounced within the LC (Fig. B1). To understand this signal better, we compute seasonal averages for the MHW and MCS composites (not shown) and find that in *wind* the subsurface maximum is strongest in autumn (March-April-May, MAM), however, it starts to develop in summer (DJF) and

extends into winter (June-July-August, JJA) while it gradually deepens throughout. This seems to be partly driven by the mean seasonal cycle along the coast of Australia, comprising a seasonal deepening of the surface mixed layer which creates a similar seasonal subsurface anomaly (Fig. B3). This process is likely enhanced during MHWs and weakened during MCS due to the overall vertical displacement of isotherms. The seasonality is driven from upstream, where a positive sea level anomaly, built up by monsoonal winds during November and December, emerges during DJF and subsequently propagates poleward along the coast (downwelling component), which also is thought to be the driver of the LC seasonality (Ridgway and Godfrey 2015).

As suggested by the surface NNI timeseries (Fig. 4), the vertical composites also show that warm anomalies are associated with fresh (negative) salinity anomalies and vice versa. These extend over the upper 200 m in *hindcast*, while the sign of the anomalies reverses below, with slightly stronger anomalies at depth for MCSs compared to MHWs. In the LC band MHW composite anomalies are slightly larger at depth. Phillips et al. (2005) showed from observations that the fresh anomaly in 2000 extended down to approximately 180 m, thus being consistent with the composites in the model. Salinity depicts an overall higher contribution from the wind forcing, which again is responsible for the depth extent. As for temperature the anomalies at depth, including the sign reversal, can be explained in terms of a wind-dominated vertical displacement of the isohalines. Because salinity has a subsurface maximum at about 200 m, a deepening of the isohalines (in case of a MCS) leads to positive anomalies above and negative anomalies below the maximum (see schematic in Fig. 13).

The imprint of the LC becomes apparent in the meridional velocity, which shows enhanced southward flow, i.e. negative anomalies, associated with MHWs across the upper 200 m. MCSs are associated with northward anomalies, i.e. a weakening of the LC, which are slightly smaller in magnitude than for MHWs and are significant in the upper 100 m only. Generally, the velocity

378 signal is fully driven by wind forcing, with non-significant thermohaline contributions of opposite  
379 sign. The vertical composites for the LC band only, show a significant reversal of velocity anomaly  
380 lies below approximately 180 m, suggesting that these signals are compensated by offshore signals  
381 when averaging over the NNI box. The LUC is located within a depth range of 200 – 600 m (e.g.  
382 Domingues et al. 2007; Furue et al. 2017). This suggests a possible coupling between the LC  
383 and underlying LUC as proposed in previous studies (McCreary et al. 1986; Kundu et al. 1986;  
384 Domingues et al. 2007; Furue et al. 2017), however, these processes as well as the drivers of the  
385 LUC are still not well understood. While a more detailed analysis of the coupling and also the in-  
386 teraction of the boundary currents with the interior flow with respect to the depth-extent of extreme  
387 events would likely be very insightful, this is beyond the scope of this study.

#### 388 *b. Watermass characteristics*

389 Ningaloo Niño has been linked to LC variability (e.g. Feng et al. 2013) and associated advection  
390 of warmer and fresher waters from upstream southward along the coast of Western Australia. The  
391 waters transported by the LC are sourced from the ITF and from eastward geostrophic surface  
392 flow from the interior eastern Indian Ocean toward the western Australian coast (Menezes et al.  
393 2013, 2014). An analysis of the water mass properties in TS-space can provide additional insight  
394 to the origin of water associated with extreme events and ultimately on the relevant drivers. A TS-  
395 diagram of the NNI properties (0 – 800 m) (Fig. 6a,b) shows a stronger influence of the fresh ITF  
396 waters associated with maximum anomalies during MHWs, while MCSs show a slight tendency  
397 toward higher salinity.

398 Spatial averaging as done for the NNI might blur the water mass characteristics. Therefore,  
399 Fig. 6c,d shows all data points for the composites within the LC band (see Fig. 1a). The influence  
400 of fresh Indonesian Sea waters is apparent more clearly. This leads to lower densities that are about

0.1 kgm<sup>-3</sup> lighter than during MCSs, which in turn likely impact the LC strength. Fresher/lighter surface waters transported by the LC may enhance the cross-shelf density gradient and thus drive a stronger southward flow (Feng et al. 2015), which is consistent with the velocity anomalies described earlier (Fig. 5). Feng et al. (2015) showed that the fresh anomaly during the 2010/2011 Ningaloo Niño contributed about 30% to the observed anomalous strengthening of the LC.

### *c. Spatial composites*

To relate regional variability represented by the NNI with large-scale ocean patterns, spatial composites of temperature and salinity are derived for MHWs and MCSs at different depth levels (Fig. 7). To avoid repetition, only MHW composites are shown and discussed in this section. Composites of MCSs however, show comparable features of opposite sign (Fig. B2).

Surface temperature anomalies in *hindcast* show the largest values adjacent to the coast of Western Australia, however, they are part of a large-scale patch of warm anomalies extending offshore and northward to about 15°S as well as southward around Cape Leeuwin. The characteristic wedge-shape was described to reflect the seasonal evolution of the WES feedback along the northeast flank of the Mascarene (subtropical) High (Marshall et al. 2015). A comparison to *buoyancy* (Fig. 7) suggests that buoyancy forcing is the dominant driver of these surface anomalies, while only small anomalies are present in *wind*. Here it is important to understand the design of the sensitivity experiments; while the winds in *buoyancy* will not show anomalous signals due to the applied repeat-year forcing, the heat fluxes of the forcing product will still reflect increased heat fluxes into the ocean as a response to decreased wind (in the real world). Hence, we learn that ultimately heat fluxes drive the observed SST pattern, however, the wind can still be important in driving these anomalous heat fluxes. We can then conclude that in this instance the wind has an



indirect effect (only via heat fluxes) on SST rather than a direct one through e.g. a downwelling of isotherms.

At depth ( $\sim 70$ -200 m) strong anomalies appear in the tropical Indian Ocean and throughout the Indonesian archipelago, with maximum anomalies being found in the equatorial western Pacific, where the Mindanao Current feeds the ITF. In contrast to the surface, the wind forcing dominates at depth, which is consistent with the vertical structure of the NNI described earlier (Fig. 5). Here the experiment indicates that the wind has a direct effect on the temperature anomalies, which, again, does not rule out the potential importance of surface buoyancy fluxes in setting up these wind-driven anomalies. In *hindcast* and *wind*, maximum positive anomalies at the 134 m level (Fig. 7) stretch along the continental slope from northern Western Australia into the NNI region. Consistent with the in-situ profiles in the NNI box, composites of the mean vertical profile over the continental slope at  $120^{\circ}\text{E}$  (not shown) indicate a vertical displacement of the thermocline (here  $20^{\circ}$ -isotherm was used) by about 3 – 4 m associated with MHWs (shallower thermocline) and MCS (deeper thermocline), which creates the observed subsurface maximum. Similar conditions are found in the Makassar Strait, therefore we conclude that these large-scale subsurface anomalies reflect the influence of the western Pacific winds on the thermocline depth in the Maritime continent as proposed by other studies previously. For example Marshall et al. (2015) find a positive correlation of the surface NNI with western Pacific ocean heat content (based on reanalysis data) over the upper 200 m. While it is commonly accepted that these signals propagate through the Maritime continent, the lack of observational data in combination with the complex geometry and circulation lead to very few studies that actually investigate the large-scale vertical structure in that region. The vertical displacement within the NNI box is larger with  $\sim 30$  m at  $24^{\circ}\text{S}$ , however, the temperature gradient within the thermocline is not as large as further upstream. Furthermore, these are composite values and displacements can thus vary from event to event.

447 The results above showed that generally fresh anomalies accompany strong MHWs. The spatial  
448 composites reveal a large-scale surface intensified fresh (low salinity) anomaly extending across  
449 the ITF region into the South China Sea. Intensified anomalies are also present along the coast  
450 of northern Australia. Fresh anomalies gradually decrease with depth, with the exception of the  
451 coastal region of Sumatra where a subsurface fresh anomaly is present at 78m. This signal is  
452 likely again associated with a deepening of the thermocline. Along the coast of Australia, fresh  
453 anomalies extend down to approximately 200m depth, consistent with the NNI vertical structure,  
454 which reflects the depth range influenced by the LC.

## 455 **6. Case study: 2010/2011 Ningaloo Niño**

456 The 2010/2011 Ningaloo Niño event is used as a case study. The surface and mixed-layer  
457 properties of this event have been investigated extensively in previous studies (e.g. Kataoka et al.  
458 2014; Benthuisen et al. 2014; Marshall et al. 2015). This study further elaborates on the evolution  
459 of the vertical structure extending below the mixed layer and associated large-scale spatial surface  
460 and subsurface patterns. Furthermore, choosing this event can help to ground-truth the model's  
461 skill in representing MHW events in the region. The 2010/2011 event has been of unprecedented  
462 strength with drastic ecological impacts (e.g. Wernberg et al. 2013, 2016). Due to the seasonally  
463 varying threshold applied in this study for detecting extremes and likely the use of monthly model  
464 output, the event starts in October 2010 and lasts 20 months until May 2012. However, we focus  
465 on the period from October 2010 to June 2011, since the largest anomalies are typically found  
466 during austral summer (Marshall et al. 2015; Kataoka et al. 2014) and the 2011/2012 event may  
467 have had different drivers. Nevertheless, the length of the detected event suggests, that the region  
468 experienced warm anomalies over a long period, even if not officially identified as MHW for the  
469 whole period in daily satellite.

470 *a. Spatial patterns*

471 The average spatial temperature patterns during the 2010/2011 MHW (Fig. 8) are very similar to  
472 the MHW composite patterns with wedge-like surface temperature anomalies in the southeastern  
473 Indian Ocean and a strong subsurface anomaly in the tropical Indian Ocean and the ITF region.  
474 Salinity also depicts large-scale negative surface anomalies, which are particularly pronounced in  
475 the Makassar Strait and along the northern Australian coast. At 78 m depth a strong fresh anomaly  
476 is found along the coast of Java, where positive salinity anomalies are present at the surface. While  
477 the surface fresh signal is controlled by thermohaline forcing, this subsurface anomaly is wind-  
478 forced (not shown but also apparent in composite, Fig. 7).

479 *b. Time evolution and vertical structure*

480 The temporal evolution of the 2010/2011 Ningaloo Niño has been investigated previously  
481 amongst others by Benthuisen et al. (2014) who focused on the near surface temperature  
482 (0 – 130m). The authors suggested that a remotely forced strengthening of the LC contributed  
483 roughly 2/3 and a local positive air-sea flux into the ocean roughly 1/3 to the rise in temperatures.  
484 We are investigating the vertical structure of the event across the upper 800m in the NNI box and  
485 the relative importance of buoyancy versus wind forcing.

486 The *hindcast* shows an initial warm temperature and southward meridional velocity anomaly  
487 across the upper 250m in October 2010 (Fig. 9b,d), indicating an initial strengthening of the LC,  
488 which is in agreement with Marshall et al. (2015). The JRA-55 meridional wind averaged over the  
489 NNI box (Fig. 9a) shows northerly wind anomalies during this time, opposing the mean southerly  
490 winds and thus contributing to a strengthening of the southward flowing LC. Correspondingly,  
491 the signal is dominant in *wind*, while only a very minor initial temperature anomaly is observed in

492 *buoyancy*. A high latent heat flux (Fig. 9a) indicates that the ocean is losing heat to the atmosphere  
493 at this point.

494 While surface temperatures in *wind* remain almost unchanged throughout the summer, a strong  
495 warming of the surface layer is observed in *buoyancy* from November onward, reaching its maxi-  
496 mum in March, which is mirrored in *hindcast*. This is the time period when the event is detected as  
497 a MHW in the daily satellite SST data. Furthermore, this is consistent with previous studies which  
498 suggest that the buoyancy forcing plays a key role in amplifying the surface signal via the acti-  
499 vation of the WES feedback (Benthuisen et al. 2014; Kataoka et al. 2014; Marshall et al. 2015).  
500 Continuous northerly wind anomalies from October through to February, when they reach their  
501 maximum amplitude, maintained a strengthened LC and a wind-driven contribution to the warm-  
502 ing event. However, without further analysis it cannot be quantified how much local wind forcing,  
503 for example through a weakening of the coastal upwelling component driven by a weakening of  
504 the southerly winds versus a remotely driven wind signal contributes to the warming. A transition  
505 from northerly to southerly winds and thus a strengthening of the absolute wind occurs in March,  
506 associated with a rapid increase in latent heat flux, which marks the onset of declining surface  
507 anomalies.

508 Salinity does not show an anomaly in October in *hindcast*. The sensitivity experiments sug-  
509 gest that a wind-induced freshening was counterbalanced by buoyancy-forced positive anomalies.  
510 From January onward negative salinity anomalies also develop in *buoyancy*, resulting in a strong  
511 freshening in *hindcast*. Thus, the freshening cannot solely be attributed to a wind-driven increased  
512 southward transport of fresh and warm waters by the LC. Marshall et al. (2015) attribute the local  
513 SST amplification to the onset of the WES feedback to the northwest of Australia, which also pro-  
514 motes increased rainfall in January and February. This mechanism can explain the thermohaline

515 contribution to the fresh anomaly in the surface layer, which we will also see below when looking  
516 at the spatial evolution (10).

517 Temperature and salinity anomalies in *buoyancy* during the peak of the MHW are limited to the  
518 upper 500m. In *wind* a subsurface temperature anomaly peak starts developing from February  
519 onward, together with a deepening and strengthening of the fresh anomaly in the upper 250m,  
520 with a maximum amplitude in May. The combination of surface thermohaline and subsurface  
521 wind-driven warming signal is expressed in *hindcast*, where in May and June higher anomalies  
522 are found subsurface. Positive temperature anomalies extend down to about 600 – 700m and  
523 gradually increase throughout the event. Initially, the salinity anomalies also extend to this depth  
524 in *wind*, however, they change sign below 250m from February onward.

525 Our results are in agreement with previous studies and suggest that an initial wind-driven  
526 strengthening of the LC sets up a positive temperature anomaly in October. Marshall et al. (2015)  
527 show that a positive SSH anomaly is propagating through the Maritime continent from September  
528 onward, reaching the northern shelf of Western Australia in October, which is consistent with a  
529 deepening of the thermocline found in the model. Our results show that the resulting temperature  
530 anomaly extends over the upper 250m. Buoyancy forcing amplifies the surface anomalies from  
531 November onward with maximum anomalies being reached in March. A transition from northerly  
532 wind anomalies and associated increase in latent heat flux in March likely contributed to the sur-  
533 face cooling thereafter. However, wind forcing drives a subsurface extension of the MHW, which  
534 is likely connected to the large-scale subsurface anomaly found in the Indonesian Sea (Fig. 8).

### 535 *c. Time evolution of the spatial structure*

536 As a next step, monthly spatial surface temperature and salinity anomalies during the 2010/2011  
537 MHW are investigated (September 2010 - August 2011; Fig. 7). In September 2010, largest

538 anomalies (temperature and salinity) are found between 0 – 15°S and in particular along the coast  
539 of Java. These could be remnants of the anomalous strong Indian summer (boreal) monsoon in  
540 2010, influenced by a negative Indian Ocean Dipole in combination with La Niña, that led to  
541 anomalous rainfall in the eastern Indian Ocean and Indonesian Seas (Feng et al. 2013, 2015).

542 From October onward anomalies south of 15°S intensify forming a warm patch off the coast  
543 of northwestern Australia in November and reaching the coastline in December, which likely  
544 reflects the onset of the WES feedback as described by Marshall et al. (2015). The temperature  
545 anomaly amplifies in the consecutive months associated with a fresh lens forming to the northwest  
546 of Australia in January and February (Fig. 10, bottom). The latter can explain the onset of the  
547 observed surface freshening in *buoyancy* in the NNI box (Fig. 9).

548 From January onward the MHW propagates southward along the coast, passing through the NNI  
549 box. The flow becomes unstable in the southern part of the NNI box and partly detaches from the  
550 coast, carrying the anomalies offshore, in a region that is generally characterized by large eddy-  
551 activity. Domingues et al. (2006) showed based on a modeling study, that 70% of the warming of  
552 a vast area in the southeast Indian Ocean (east of 107°) is driven by eddy fluxes originating from  
553 the LC. Thus, the temperature anomalies at depth (200 – 300m) as presented in this study may  
554 not just have implications for the coastal region but also for the off-shore region. Furthermore,  
555 the spatial evolution shows that warm anomalies also continue to propagate along the coast and  
556 around Cape Leeuwin following the coastal wave guide.

557 In January a tongue of cold anomalies forms along the outer archipelago extending to the north  
558 Australian coast, where it propagates into the archipelago as well as southward, reaching the NNI  
559 box in May and likely contributing to the damping of the MHW. This pattern is likely driven by  
560 the monsoon-related seasonal reversal of winds. However, warm anomalies persist along and off  
561 the coast of Western Australia as indicated by the NNI.

## 7. Connection to large-scale climate variability

The circulation and thermohaline water mass properties in the eastern Indian Ocean are affected by large-scale climate modes acting on decadal time scales, such as the IPO as well as on interannual time scales, like ENSO. The ITF plays an important role in the coupling between the Pacific and the Indian Ocean (Sprintall et al. 2014; Lee et al. 2019; Hu et al. 2019). Improving our understanding of the connection between these large-scale patterns, some of which have well known evolution or precursors, and the variability associated with Ningaloo Niño/Niña is essential for prediction and adaptation purposes.

Hovmoeller plots of the temperature and salinity NNI (Fig. 11a,b) show interannual variability across the upper 600m (much weaker below therefore not shown) and suggest a 2-layer system, which is particularly pronounced in salinity (as suggested by vertical composites already). In order to reduce the noise and eliminate small scale signals in the vertical, temperature and salinity are averaged over the upper (0 – 200 m) and lower (200 – 600 m) layers and are shown as time series together with the ONI (Fig. 11c-f). We find a significant negative correlation of -0.6 ( $p < 0.01$ ) between the upper layer temperature anomaly and the ONI (over full time period), while it is even slightly higher (-0.69,  $p < 0.01$ ) in the lower layer. Similarly, the correlation coefficient for the upper layer salinity is 0.5 ( $p < 0.01$ ) while it is -0.55 ( $p < 0.01$ ) for the lower layer. The opposing signs of the correlations in salinity could again be attributed to the general vertical structure with a salinity maximum around 200 m. The slightly weaker correlation in the upper layer likely reflects the influence of local, non-ENSO related processes, such as the WES feedback on the surface layer.

There are no obvious shifts during a specific IPO phase in upper layer temperature, while in the lower layer large positive anomalies seem to be more frequent during negative IPO phases such as

for example in the mid-1970s and mid-2000s onward. These events are also associated with large positive salinity anomalies in the lower layer. However, it should also be noted that anomalies during these events seem to be correlated particularly well with the ONI. In contrast to the lower layer, it is the 4 largest negative salinity events in the upper layer that occurred during negative IPO, while there is a tendency to more positive anomalies from the late 1970s to roughly 2000s when the IPO was in a positive phase. These salinity signals in the upper layer are consistent with Hu et al. (2019) who have shown that the IPO/PDO has strong impacts on salinity in the southeast Indian Ocean, with positive (negative) salinity anomalies generally occurring during negative (positive) IPO and ENSO phases.

Correlation coefficients of the NNI and the IPO tripole index are very similar to the correlations with the ONI index (see Table 2), suggesting that the overall correlation can be attributed to the interannual ENSO variability that is also reflected in the IPO index. However, as mentioned above our results indicate that the IPO does modulate signals in the NNI box on top of ENSO, in particular in the lower layer. This would be consistent with findings by Li et al. (2020), that the thermocline in Makassar Strait shows larger interannual variability with periods of 2-7 years and the sub-thermocline large variability on decadal timescales ( $> 10$  years). Furthermore, we find periods of higher correlations vs. periods of lower correlations when performing a running mean correlations with window sizes of 10 and 20 years (not shown). Generally, it is difficult to strictly separate the impacts of the IPO and ENSO on the NNI region without a more detailed analysis, which lies beyond the scope of this study.

It has been shown that La Niña events can favor the development of Ningaloo Niño, however, many events also occur during neutral or positive, i.e. La Niño, phases (Kataoka et al. 2014; Marshall et al. 2015, also see Table 1). Here we investigate the depth structure of selected MHWs that were associated with either a clear negative (La Niña) or positive (El Niño) ONI (Fig. 12).



609 The events during El Niño show a strikingly different vertical structure with positive temperature  
610 anomalies being limited to the surface layer, where the buoyancy forcing seems to be the sole  
611 driver, while events associated with La Niña are characterized by positive temperature anomalies  
612 extending to much greater depth. As found in the composites, the signal at depth is wind-driven  
613 while both forcing components contribute to the surface signal. Consistently, only the La Niña  
614 events show a freshening across the upper 200 m and a strengthening of the LC associated with the  
615 temperature anomalies.

616 By providing insight into the depth structure, these results therefore complement and augment  
617 our knowledge based on results of Kataoka et al. (2014) and Marshall et al. (2015). In particular,  
618 Kataoka et al. (2014) distinguished between locally amplified and remotely forced events and  
619 define the coastal wind index (CWI) as a measure of local forcing. We derive the CWI by averaging  
620 the meridional ocean surface stress over the NNI box. The mean CWI value is derived for each  
621 event (see Table 1). The CWI for the El Niño, surface-intensified events in our results is strongly  
622 positive, indicating northerly wind anomalies which lead to an overall decrease of wind speed and  
623 therefore a reduced latent heat flux to the atmosphere explaining that the signal is only visible in  
624 *buoyancy*. The CWI is weak in the 1976 event and on average also during the 2000 and 2011 event,  
625 however, the maximum value during the peak of the MHW is high with 4.15 in January 2010 and  
626 6.39 in February 2011. The depth-extent of the anomalies in these selected events agrees with our  
627 earlier discussion for the composite profiles and spatial patterns at depth in that these anomalies  
628 are driven by a large-scale vertical displacement of the thermocline, likely induced in the western  
629 Pacific by increased easterly wind stress during negative ENSO phases.

## 8. Discussion and conclusions

We utilized output of a global ocean general circulation model ( $1/4^\circ$ ) from 1958-2016 to investigate temporal and spatial characteristics of Ningaloo Niño (MHW) and Niña (MCS) with particular focus on the depth structure. Sensitivity experiments are used to investigate the contributions of buoyancy versus wind forcing to the observed patterns. A Ningaloo Niño index is derived also for salinity, in addition to temperature. A comparison to the leading EOF mode, shows that the salinity index also represents the regional variability well.

A composite analysis shows that Ningaloo Niño/Niña is associated with large-scale subsurface temperature anomalies that extend from the western Pacific across the Maritime Continent into the tropical eastern Indian Ocean which also reflect as subsurface maximum/minimum in the vertical NNI profiles. SSTs exhibit the characteristic wedge-shape pattern with maximum anomalies along the coast of Western Australia reflecting the WES feedback being active off the coast of northwestern Australia (Kataoka et al. 2014; Marshall et al. 2015). Salinity shows a large-scale surface anomaly across the eastern Indian Ocean and the Indonesian Seas, with a weaker subsurface expression. The sensitivity experiments reveal that surface anomalies are dominated by buoyancy forcing, while the subsurface anomalies mainly are wind-driven.

Strong symmetry is found between Ningaloo Niño and Ningaloo Niña composites of the vertical structure within the NNI box (Fig. 5, Fig. 13), suggesting common driving processes for positive and negative extremes. Temperature anomalies are largest in the surface layer, where thermohaline forcing is the major contributor. The wind-forced run, however, reveals a subsurface temperature maximum anomaly and is generally responsible for extending the anomalies to greater depth. We suggest that the large-scale anomalies are driven by vertical displacements of isotherms (Fig. 13c) while a seasonal downwelling component, generated along the northern Australian coast by mon-

653 soonal winds and then propagating poleward along the coast of Western Australia is also at play  
654 in the Ningaloo region.

655 Composites show that significant temperature anomalies extend to a depth of 300 m, which inter-  
656 estingly is deeper than the depth of the LC of about 200 m. Furthermore, the anomalies at depth are  
657 even more pronounced within the LC and salinity and meridional velocity anomalies show a clear  
658 change of sign below about 200 m depth, reflecting the transition from the LC and the LUC below.  
659 A coupling between the two has been suggested (Furue et al. 2017) via gradual downwelling at the  
660 interface, however, little is known still about the dynamics of the system. The anomalies are con-  
661 sistent with a vertical displacement of isotherms and isohalines and the respective in-situ profiles  
662 of temperature and salinity. However, in order to fully understand the presented depth structure of  
663 anomalies associated with Ningaloo Niño/Niña, a more thorough analysis of the coupling between  
664 the two boundary currents and the role of the interior flow feeding into these is needed.

665 We find that Ningaloo Niños in 2000 and 2011 are unprecedented compound events, where long-  
666 lasting high temperatures are accompanied by extreme freshening of similar magnitude, which is  
667 unprecedented since 1980. These freshening events have previously been described and connected  
668 to strong La Niña forcing by Phillips et al. (2005) and Feng et al. (2013, 2015) for the 2000  
669 and 2011 event respectively, however only the latter was discussed in direct relation to MHWs.  
670 Our analysis shows that the fresh anomalies coincide with a negative phase of the IPO, which  
671 is consistent with results by Hu et al. (2019), who show that negative salinity anomalies in the  
672 southeast Indian Ocean generally occur during negative phases of the Pacific Decadal Oscillation  
673 (a more regional phenomena as part of the IPO) and ENSO, while positive anomalies occur during  
674 their positive phases. The salinity NNI reveals two freshening events of similar magnitude and  
675 length in the 1960s and 1970s again associated with a negative IPO phase, however only the latter  
676 coincides with a persistent La Niña phase. Nevertheless, MHWs are detected during both events,

though not as persistent as in 2000 and 2011, which might be attributed to the general background warming of the ocean over the last few decades. Although the 1962 event shows a temperature anomaly above  $1.5^{\circ}\text{C}$ , which is on the same order of magnitude as the 2000 event. Generally, both, upper layer temperature and salinity, show significant correlations ( $\sim 0.5$ - $0.6$ ,  $p < 0.01$ ) with the ONI index, where wind forcing is the major contributor (see Table 2). Correlations with the IPO index are only slightly higher than with the ONI, suggesting that these arise from the interannual ENSO component that is embedded in the unfiltered IPO index.

The 2011 Ningaloo Niño has been investigated in detail in recent years (Feng et al. 2013; Kataoka et al. 2014; Marshall et al. 2015). The observation based study by Marshall et al. (2015) shows that the initial warming is driven by increased poleward advection in Oct-Dec 2010, followed by an intensification of surface anomalies via anomalous heat fluxes. Our analysis of the vertical, monthly evolution of the 2011 event is in agreement with these findings and indicates that the ocean model and the associated sensitivity experiments are performing well. In this study, we shed light on the vertical structure and evolution of the event and show that the strongest anomalies are found in a thin surface layer, however, positive temperature anomalies of about  $1^{\circ}\text{C}$  extent down to 250 m depth and anomalies around  $0.5^{\circ}\text{C}$  to 600 m depth in the composites. Our sensitivity experiments show that this subsurface signal is wind-driven and develops in austral summer extending into autumn/winter driven by a downwelling anomaly that propagates along the coast seasonally. During MHWs and MCSs this signal is enhanced or muted, respectively.

Information about the vertical extent of ocean extremes will be indispensable for impact assessment and adaptation strategies. One future step could be to define different categories of vertical structures associated with MHWs off the western Australia coast as recently done in the Tasman Sea (Elzahaby et al. 2019). Our analysis shows that there are significant differences between events, in particular events associated with negative ENSO phases have a greater depth extent

701 compared to events during a positive or neutral phase. The latter are dominated by buoyancy forc-  
702 ing which acts on the surface layer only and is likely driven through local feedback mechanisms.  
703 These results augment results by Kataoka et al. (2014) who proposed the existence of locally vs.  
704 non-locally amplified events based on surface data. Model output with higher temporal and spatial  
705 resolution would be preferable to expand our analysis. A 5-daily mean output for *hindcast* is cur-  
706 rently generated as well as a configuration with a high-resolution ( $1/20^\circ$ ) nest for the Indo-Pacific  
707 region.

708 A recent study Pilo et al. (2019) suggests that all models have biases in MHW intensity, fre-  
709 quency and duration, however, eddy-permitting models are able to produce global spatial patterns  
710 of MHWs that are comparable to observed spatial patterns. Our results confirm this. Furthermore,  
711 our analysis is likely only valid for larger events, since short events in the order of days are not  
712 resolved temporally unless they appear in high frequency, which would then be expressed in the  
713 monthly mean field. However, Kataoka et al. (2014) and Marshall et al. (2015) show in their com-  
714 posite analysis that significant anomalies start to develop in October already associated with the  
715 development of northeasterly wind anomalies. This can explain why for example the 2010/2011  
716 begins in October in our analysis. Because the amplitudes are likely underestimated and duration  
717 (compared to detection based on daily data) of events overestimated, we did not put emphasis on  
718 the absolute values but rather tried to focus on the spatial and vertical relative structures. Our anal-  
719 ysis has shown, in agreement with Marshall et al. (2015), that in order to assess large-scale drivers  
720 and spatial patterns associated with strong events, such as the 2011 Ningaloo Niño, the evolution  
721 over several month has to be studied, even if the actual event is much shorter. Therefore, even at  
722 monthly output, our model has proven to be an adequate and valuable tool.

723 Furthermore, the sensitivity experiments used here were able to distinguish between important  
724 drivers for the depth structure in the Ningaloo region and reflected proposed mechanisms by pre-

vious individual studies. While some of the presented results seem to 'only' confirm results previously published, we believe that in addition to providing important insight into the depth structure of extreme events in the southeast Indian Ocean, this study also serves as a proof-of-concept that the global ocean models in combination with the sensitivity experiments is able to capture the relevant processes at play. This will serve as a basis for future studies with this model at higher temporal and spatial resolution. Due to sparse observations and the complex circulation in the Maritime Continent, investigations of the vertical profile of the ITF and its variability have been limited. It will be interesting to explore connections between the ITF and the upper southeastern Indian Ocean in the future. Our analysis suggests for example that the depth range between 200-600 m is more strongly correlated to large-scale processes while the upper layer is also modulated by local processes.

*Acknowledgments.* Use of the following datasets is gratefully acknowledged: Hadley Centre Sea Ice and Sea Surface Temperature (HadISST) accessed at <https://www.metoffice.gov.uk/hadobs/hadisst/data/download.html>, In situ analysis system (ISAS-15) tool accessed at <https://www.seanoe.org/data/00412/52367/>, and global ocean gridded L4 sea surface heights, which is made available by E.U. Copernicus Marine Service (CMEMS) and can be downloaded under [https://resources.marine.copernicus.eu/?option=com\\_csw&task=results?option=com\\_csw&view=details&product\\_id=SEALEVEL\\_GLO\\_PHY\\_L4\\_REP\\_OBSERVATIONS\\_008\\_047](https://resources.marine.copernicus.eu/?option=com_csw&task=results?option=com_csw&view=details&product_id=SEALEVEL_GLO_PHY_L4_REP_OBSERVATIONS_008_047). The Oceanic Nino Index (ONI) was downloaded <https://psl.noaa.gov/data/climateindices/list/#ONI>. The integration of the OGCM simulations was performed at the North-German Supercomputing Alliance (HLRN) and the Computing Centre at Kiel University. The authors thank two anonymous reviewers for their constructive feedback that helped improve an earlier version of the manuscript. Thank you to

748 Susan Wijffels for a helpful discussion. SR was supported by a Feodor-Lynen Fellowship by  
749 the Alexander von Humboldt Foundation and the WHOI Postdoctoral Scholar program. GG  
750 was supported by the Office of Naval Research under project number N-00014-19-12646).  
751 Support from the James E. and Barbara V. Moltz Fellowship for Climate-Related Research is  
752 gratefully acknowledged. PW was supported through grant IndoArchipel from the Deutsche  
753 Forschungsgemeinschaft (DFG) as part of the Special Priority Program (SPP)-1889 "Regional  
754 Sea Level Change and Society" (SeaLevel).

## 755 APPENDIX A

### 756 Supporting tables

## 757 APPENDIX B

### 758 Supporting figures

## 759 References

- 760 Barnier, B., and Coauthors, 2006: Impact of partial steps and momentum advection schemes in a  
761 global ocean circulation model at eddy-permitting resolution. *Ocean Dynamics*, **56** (5-6), 543–  
762 567, doi:10.1007/s10236-006-0082-1.
- 763 Behrens, E., D. Fernandez, and P. Sutton, 2019: Meridional oceanic heat transport influences  
764 marine heatwaves in the tasman sea on interannual to decadal timescales. *Frontiers in Marine*  
765 *Science*, **6** (APR), 1–17, doi:10.3389/fmars.2019.00228.
- 766 Benthuisen, J., M. Feng, and L. Zhong, 2014: Spatial patterns of warming off western australia  
767 during the 2011 ningaloo niño: Quantifying impacts of remote and local forcing. *Continental*  
768 *Shelf Research*, **91**, 232–246, doi:10.1016/J.CSR.2014.09.014.

- 769 Benthuisen, J. A., E. C. J. Oliver, M. Feng, and A. G. Marshall, 2018: Extreme marine warming  
770 across tropical australia during austral summer 2015-2016. *Journal of Geophysical Research:*  
771 *Oceans*, **123** (2), 1301–1326, doi:10.1002/2017JC013326.
- 772 Clarke, A. J., and X. Liu, 1994: Interannual sea level in the northern and eastern indian  
773 ocean. *Journal of Physical Oceanography*, **24** (6), 1224–1235, doi:10.1175/1520-0485(1994)  
774 024<1224:islitn>2.0.co;2.
- 775 Domingues, C. M., M. E. Maltrud, S. E. Wijffels, J. A. Church, and M. Tomczak, 2007: Simulated  
776 lagrangian pathways between the leeuwin current system and the upper-ocean circulation of the  
777 southeast indian ocean. *Deep Sea Research Part II: Topical Studies in Oceanography*, **54** (8-10),  
778 797–817, doi:10.1016/J.DSR2.2006.10.003.
- 779 Domingues, C. M., S. E. Wijffels, M. E. Maltrud, J. A. Church, and M. Tomczak, 2006: Role  
780 of eddies in cooling the leeuwin current. *Geophysical Research Letters*, **33** (5), L05 603, doi:  
781 10.1029/2005GL025216.
- 782 Elzahaby, Y., A. Schaeffer, and P. J. Sutton, 2019: Observational insight into the subsur-  
783 face anomalies of marine heatwaves. *Frontiers in Marine Science*, **6** (December), 1–14, doi:  
784 10.3389/fmars.2019.00745.
- 785 Fabienne, G., 2012: Isas-tool version 6 : Method and configuration. *LPO-12-02*, doi:10.13155/  
786 22583.
- 787 Feng, M., J. Benthuisen, N. Zhang, and D. Slawinski, 2015: Freshening anomalies in the indone-  
788 sian throughflow and impacts on the leeuwin current during 2010-2011. *Geophysical Research*  
789 *Letters*, **42** (20), 8555–8562, doi:10.1002/2015GL065848.



- 790 Feng, M., A. Biastoch, C. Böning, N. Caputi, and G. Meyers, 2008: Seasonal and interannual  
791 variations of upper ocean heat balance off the west coast of australia. *Journal of Geophysical*  
792 *Research: Oceans*, **113** (C12), doi:10.1029/2008JC004908.
- 793 Feng, M., M. J. McPhaden, S. P. Xie, and J. Hafner, 2013: La niña forces unprecedented leeuwin  
794 current warming in 2011. *Scientific Reports*, **3**, 1–9, doi:10.1038/srep01277.
- 795 Feng, M., G. Meyers, A. Pearce, and S. Wijffels, 2003: Annual and interannual variations of  
796 the leeuwin current at 32°S. *Journal of Geophysical Research*, **108** (C11), 3355, doi:  
797 10.1029/2002JC001763.
- 798 Feng, X., and T. Shinoda, 2019: Air-sea heat flux variability in the southeast indian ocean and  
799 its relation with ningaloo niño. *Frontiers in Marine Science*, **6**, 266, doi:10.3389/fmars.2019.  
800 00266.
- 801 Fichefet, T., and M. A. Maqueda, 1997: Sensitivity of a global sea ice model to the treatment  
802 of ice thermodynamics and dynamics. *Journal of Geophysical Research: Oceans*, **102** (C6),  
803 12 609–12 646, doi:10.1029/97JC00480.
- 804 Frölicher, T. L., and C. Laufkötter, 2018: Emerging risks from marine heat waves. *Nature Com-*  
805 *munications*, **9** (1), 650, doi:10.1038/s41467-018-03163-6.
- 806 Furue, R., and Coauthors, 2017: On the leeuwin current system and its linkage to zonal flows in the  
807 south indian ocean as inferred from a gridded hydrography. *Journal of Physical Oceanography*,  
808 **47** (3), 583–602, doi:10.1175/JPO-D-16-0170.1.
- 809 Gordon, A., 2005: Oceanography of the indonesian seas and their throughflow. *Oceanography*,  
810 **18** (4), 14–27, doi:10.5670/oceanog.2005.01.

811 Gordon, A. L., B. A. Huber, E. J. Metzger, R. D. Susanto, H. E. Hurlburt, and T. R. Adi, 2012:  
 812 South china sea throughflow impact on the indonesian throughflow. *Geophysical Research Let-*  
 813 *ters*, **39** (11), n/a–n/a, doi:10.1029/2012GL052021.

814 Gordon, A. L., and Coauthors, 2010: The indonesian throughflow during 2004–2006 as observed  
 815 by the instant program. *Dynamics of Atmospheres and Oceans*, **50** (2), 115–128, doi:10.1016/j.  
 816 dynatmoce.2009.12.002.

817 Griffies, S. M., and Coauthors, 2009: Coordinated ocean-ice reference experiments (cores). *Ocean*  
 818 *Modelling*, **26** (1-2), 1–46, doi:10.1016/j.ocemod.2008.08.007.

819 Gruenburg, L., and A. Gordon, 2018: Variability in makassar strait heat flux and its effect on the  
 820 eastern tropical indian ocean. *Oceanography*, **31** (2), 80–87, doi:10.5670/oceanog.2018.220.

821 Henley, B. J., J. Gergis, D. J. Karoly, S. Power, J. Kennedy, and C. K. Folland, 2015: A tripole  
 822 index for the interdecadal pacific oscillation. *Climate Dynamics*, **45** (11-12), 3077–3090, doi:  
 823 10.1007/s00382-015-2525-1.

824 Hobday, A. J., and Coauthors, 2016: A hierarchical approach to defining marine heatwaves.  
 825 *Progress in Oceanography*, **141**, 227–238, doi:10.1016/j.pocean.2015.12.014, arXiv:1011.  
 826 1669v3.

827 Hobday, A. J., and Coauthors, 2018: Categorizing and naming marine heatwaves. *Oceanography*,  
 828 **31** (2), early online release, doi:10.1007/s00376-014-4097-0.

829 Hu, S., and J. Sprintall, 2016: Interannual variability of the indonesian throughflow: The  
 830 salinity effect. *Journal of Geophysical Research: Oceans*, **121** (5), 2596–2615, doi:10.1002/  
 831 2015JC011495.

- 832 Hu, S., and Coauthors, 2019: Interannual to decadal variability of upper-ocean salinity in the  
 833 southern indian ocean and the role of the indonesian throughflow. *Journal of Climate*, **32** (19),  
 834 6403–6421, doi:10.1175/JCLI-D-19-0056.1.
- 835 Jones, T., and Coauthors, 2018: Massive mortality of a planktivorous seabird in response to a ma-  
 836 rine heatwave. *Geophysical Research Letters*, **45** (7), 3193–3202, doi:10.1002/2017GL076164.
- 837 Kataoka, T., S. Masson, T. Izumo, T. Tozuka, and T. Yamagata, 2018: Can ningaloo niño/niña  
 838 develop without el niño-southern oscillation? *Geophysical Research Letters*, **45** (14), 7040–  
 839 7048, doi:10.1029/2018GL078188.
- 840 Kataoka, T., T. Tozuka, S. Behera, and T. Yamagata, 2014: On the ningaloo niño/niña. *Climate*  
 841 *Dynamics*, **43** (5-6), 1463–1482, doi:10.1007/s00382-013-1961-z.
- 842 Kataoka, T., T. Tozuka, and T. Yamagata, 2017: Generation and decay mechanisms of ninga-  
 843 loo niño/niña. *Journal of Geophysical Research: Oceans*, **122** (11), 8913–8932, doi:10.1002/  
 844 2017JC012966.
- 845 Kundu, P. K., J. P. McCreary, P. K. Kundu, and J. P. M. Jr., 1986: On the dynamics of the through-  
 846 flow from the pacific into the indian ocean. *Journal of Physical Oceanography*, **16** (12), 2191–  
 847 2198, doi:10.1175/1520-0485(1986)016<2191:OTDOTT>2.0.CO;2.
- 848 Large, W. G., and S. G. Yeager, 2009: The global climatology of an interannually varying air - sea  
 849 flux data set. *Climate Dynamics*, **33** (2-3), 341–364, doi:10.1007/s00382-008-0441-3.
- 850 Lee, T., S. Fournier, A. L. Gordon, and J. Sprintall, 2019: Maritime continent water cycle regulates  
 851 low-latitude chokepoint of global ocean circulation. *Nature Communications*, **10** (1), 1–13, doi:  
 852 10.1038/s41467-019-10109-z.

- 853 Levitus, S., T. P. Boyer, M. E. Conkright, and T. O. Brien, 1998: Noaa atlas nesdis 19 world  
 854 ocean database 1998 volume 2 : Temporal distribution of mechanical bathythermograph profiles  
 855 1998 international year of the ocean. *National Oceanographic Data Center, Ocean Climate*  
 856 *Laboratory*, **2**.
- 857 Li, M., A. L. Gordon, L. K. Gruenburg, J. Wei, and S. Yang, 2020: Interannual to decadal response  
 858 of the indonesian throughflow vertical profile to indo-pacific forcing. *Geophysical Research*  
 859 *Letters*, **47 (11)**, 1–10, doi:10.1029/2020GL087679.
- 860 Madec, G., 2016: Nemo ocean engine (2014). *Note du P\^ole de mod\`elisation de*  
 861 *l'(U+00B4)Institut Pierre-Simon Laplace*, **(27)**.
- 862 Marshall, A. G., H. H. Hendon, M. Feng, and A. Schiller, 2015: Initiation and amplification of the  
 863 ningaloo niño. *Climate Dynamics*, **45 (9-10)**, 2367–2385, doi:10.1007/s00382-015-2477-5.
- 864 McCreary, J. P., S. R. Shetye, and P. K. Kundu, 1986: Thermohaline forcing of eastern boundary  
 865 currents: With application to the circulation off the west coast of australia. *Journal of Marine*  
 866 *Research*, **44 (1)**, 71–92, doi:10.1357/002224086788460184.
- 867 Menezes, V. V., H. E. Phillips, A. Schiller, N. L. Bindoff, C. M. Domingues, and M. L. Vianna,  
 868 2014: South indian countercurrent and associated fronts. *Journal of Geophysical Research:*  
 869 *Oceans*, **119 (10)**, 6763–6791, doi:10.1002/2014JC010076.
- 870 Menezes, V. V., H. E. Phillips, A. Schiller, C. M. Domingues, and N. L. Bindoff, 2013: Salinity  
 871 dominance on the indian ocean eastern gyral current. *Geophysical Research Letters*, **40 (21)**,  
 872 5716–5721, doi:10.1002/2013GL057887.

873 Mills, K. E., and Coauthors, 2013: Fisheries management in a changing climate: Lessons from the  
 874 2012 ocean heat wave in the northwest atlantic. *Oceanography*, **26 (2)**, 191–195, doi:10.5670/  
 875 oceanog.2013.27.

876 Oliver, E. C., J. A. Benthuisen, N. L. Bindoff, A. J. Hobday, N. J. Holbrook, C. N. Mundy,  
 877 and S. E. Perkins-Kirkpatrick, 2017: The unprecedented 2015/16 tasman sea marine heatwave.  
 878 *Nature Communications*, **8 (May)**, 1–12, doi:10.1038/ncomms16101.

879 Oliver, E. C. J., and Coauthors, 2018: Longer and more frequent marine heatwaves over the past  
 880 century. *Nature Communications*, **9 (1)**, 1324, doi:10.1038/s41467-018-03732-9.

881 Pearce, A. F., and M. Feng, 2013: The rise and fall of the "marine heat wave" off western australia  
 882 during the summer of 2010/2011. *Journal of Marine Systems*, **111-112**, 139–156, doi:10.1016/  
 883 j.jmarsys.2012.10.009.

884 Phillips, H. E., S. E. Wijffels, and M. Feng, 2005: Interannual variability in the freshwater content  
 885 of the indonesian-australian basin. *Geophysical Research Letters*, **32 (3)**, L03 603, doi:10.1029/  
 886 2004GL021755.

887 Pilo, G. S., N. J. Holbrook, A. E. Kiss, and A. M. Hogg, 2019: Sensitivity of marine heatwave  
 888 metrics to ocean model resolution. *Geophysical Research Letters*, **submitted**, 2019GL084 928,  
 889 doi:10.1029/2019GL084928.

890 Rayner, N. A., D. E. Parker, E. B. Horton, C. K. Folland, L. V. Alexander, D. P. Rowell, E. C. Kent,  
 891 and A. Kaplan, 2003: Global analyses of sea surface temperature, sea ice, and night marine air  
 892 temperature since the late nineteenth century. *Journal of Geophysical Research D: Atmospheres*,  
 893 **108 (14)**, doi:10.1029/2002jd002670.

- Reynolds, R. W., and Coauthors, 2007: Daily high-resolution-blended analyses for sea surface temperature. *Journal of Climate*, **20** (22), 5473–5496, doi:10.1175/2007JCLI1824.1.
- Ridgway, K. R., and J. S. Godfrey, 2015: The source of the leeuwin current seasonality. *Journal of Geophysical Research: Oceans*, **120** (10), 6843–6864, doi:10.1002/2015JC011049.
- Short, J., T. Foster, J. Falter, G. A. Kendrick, and M. T. McCulloch, 2015: Crustose coralline algal growth, calcification and mortality following a marine heatwave in western australia. *Continental Shelf Research*, **106**, 38–44, doi:10.1016/j.csr.2015.07.003.
- Smale, D. A., and Coauthors, 2019: Marine heatwaves threaten global biodiversity and the provision of ecosystem services. *Nature Climate Change*, **9** (4), 306–312, doi:10.1038/s41558-019-0412-1.
- Smith, R. L., A. Huyer, J. S. Godfrey, and J. A. Church, 1991: The leeuwin current off western australia, 1986-1987. *Journal of Physical Oceanography*, **21** (2), 323–345, doi:10.1175/1520-0485(1991)021<0323:TLCOWA>2.0.CO;2.
- Sprintall, J., A. L. Gordon, A. Koch-Larrouy, T. Lee, J. T. Potemra, K. Pujiana, and S. E. Wijffels, 2014: The indonesian seas and their role in the coupled ocean-climate system. *Nature Geoscience*, **7** (7), 487–492, doi:10.1038/ngeo2188.
- Sprintall, J., S. E. Wijffels, R. Molcard, and I. Jaya, 2009: Direct estimates of the indonesian throughflow entering the indian ocean: 2004–2006. *Journal of Geophysical Research*, **114** (C7), C07001, doi:10.1029/2008JC005257.
- Steele, M., R. Morley, and W. Ermold, 2001: Phc: A global ocean hydrography with a high-quality arctic ocean. *Journal of Climate*, **14** (9), 2079–2087, doi:10.1175/1520-0442(2001)014<2079:PAGOHW>2.0.CO;2.

916 Stewart, K. D., and Coauthors, 2020: Jra55-do-based repeat year forcing datasets for driving  
 917 ocean–sea-ice models. *Ocean Modelling*, **147**, doi:10.1016/j.ocemod.2019.101557.

918 Tsujino, H., and Coauthors, 2018: Jra-55 based surface dataset for driving ocean–sea-ice models  
 919 (jra55-do). *Ocean Modelling*, **130 (December 2017)**, 79–139, doi:10.1016/j.ocemod.2018.07.  
 920 002.

921 Wernberg, T., D. A. Smale, F. Tuya, M. S. Thomsen, T. J. Langlois, T. de Bettignies, S. Bennett,  
 922 and C. S. Rousseaux, 2013: An extreme climatic event alters marine ecosystem structure in a  
 923 global biodiversity hotspot. *Nature Climate Change*, **3 (1)**, 78–82, doi:10.1038/nclimate1627.

924 Wernberg, T., and Coauthors, 2016: Climate-driven regime shift of a temperate marine ecosystem.  
 925 *Science*, **353 (6295)**, 2009–2012, doi:10.1126/science.aad8745.

926 Wijffels, S., G. Meyers, S. Wijffels, and G. Meyers, 2004: An intersection of oceanic waveguides:  
 927 Variability in the indonesian throughflow region. *Journal of Physical Oceanography*, **34 (5)**,  
 928 1232–1253, doi:10.1175/1520-0485(2004)034<1232:AIOOWV>2.0.CO;2.

## 929

930  
931  
932  
933  
  
934  
935  
936  
937  
938  
939  
  
940  
941  
942  
943



TABLE 1. Detected Marine Heatwaves using the 90th percentile of the modeled monthly Ningaloo Niño Index. The highlighted events agree with years identified as Ningaloo Niño years by Kataoka et al. (2014) or Marshall et al. (2015), who based their detection on DJF averages of the NNI.

| Event | Start           | End             | Duration        | Max. intensity [°C] | Max. salinity [psu] | ONI          | CWI          |
|-------|-----------------|-----------------|-----------------|---------------------|---------------------|--------------|--------------|
| 1     | 1958-Dec        | 1958-Dec        | 1 month         | 0.59                | 0.05                | 0.61         | 3.49         |
| 2     | 1959-Aug        | 1959-Sep        | 2 month         | 0.56                | 0.06                | -0.18        | -1.15        |
| 3     | <b>1961-Feb</b> | <b>1961-Feb</b> | <b>1 month</b>  | <b>0.88</b>         | <b>-0.10</b>        | <b>0.03</b>  | <b>2.33</b>  |
| 4     | <b>1962-Feb</b> | <b>1962-Feb</b> | <b>1 month</b>  | <b>1.69</b>         | <b>-0.17</b>        | <b>-0.22</b> | <b>3.69</b>  |
| 5     | 1962-Aug        | 1962-Sep        | 2 month         | 0.53                | -0.17               | -0.09        | -0.07        |
| 6     | <b>1963-Feb</b> | <b>1963-Mar</b> | <b>2 month</b>  | <b>1.37</b>         | <b>-0.38</b>        | <b>0.00</b>  | <b>1.31</b>  |
| 7     | 1963-Dec        | 1963-Dec        | 1 month         | 0.85                | -0.11               | 1.31         | 3.77         |
| 8     | <b>1973-Jan</b> | <b>1973-Jan</b> | <b>1 month</b>  | <b>0.79</b>         | <b>0.04</b>         | <b>1.84</b>  | <b>-0.66</b> |
| 9     | 1975-Nov        | 1975-Nov        | 1 month         | 0.95                | -0.24               | -1.55        | -1.77        |
| 10    | 1976-Mar        | 1976-Mar        | 1 month         | 0.83                | -0.31               | -0.73        | 0.20         |
| 11    | 1978-Mar        | 1978-Apr        | 2 month         | 1.06                | 0.05                | -0.06        | 3.19         |
| 12    | <b>1982-Nov</b> | <b>1983-Jan</b> | <b>3 month</b>  | <b>0.81</b>         | <b>0.06</b>         | <b>2.20</b>  | <b>2.88</b>  |
| 13    | 1983-May        | 1983-Jun        | 2 month         | 0.78                | -0.04               | 0.89         | 1.12         |
| 14    | 1984-Jun        | 1984-Jul        | 2 month         | 0.76                | -0.11               | -0.38        | 0.61         |
| 15    | 1984-Oct        | 1984-Oct        | 1 month         | 0.57                | -0.08               | -0.56        | 2.64         |
| 16    | 1985-Jul        | 1985-Jul        | 1 month         | 0.74                | -0.07               | -0.49        | 0.36         |
| 17    | 1988-Sep        | 1988-Oct        | 2 month         | 0.68                | 0.05                | -1.34        | 1.14         |
| 18    | 1989-Sep        | 1989-Sep        | 1 month         | 0.66                | -0.05               | -0.24        | 0.18         |
| 19    | 1996-Nov        | 1996-Nov        | 1 month         | 0.72                | -0.08               | -0.45        | 0.90         |
| 20    | <b>1997-Jan</b> | <b>1997-Jan</b> | <b>1 month</b>  | <b>0.85</b>         | <b>-0.10</b>        | <b>-0.50</b> | <b>0.40</b>  |
| 21    | 1998-May        | 1998-Jun        | 2 month         | 0.86                | 0.09                | 0.16         | 0.24         |
| 22    | 1998-Aug        | 1998-Aug        | 1 month         | 0.44                | -0.09               | -1.12        | 1.28         |
| 23    | 1999-Apr        | 1999-Aug        | 5 month         | 1.48                | -0.39               | -1.05        | 1.11         |
| 24    | <b>1999-Dec</b> | <b>2000-Apr</b> | <b>5 month</b>  | <b>1.65</b>         | <b>-0.39</b>        | <b>-1.32</b> | <b>-0.59</b> |
| 25    | 2001-Jul        | 2001-Jul        | 1 month         | 0.48                | -0.19               | -0.08        | -0.70        |
| 26    | 2008-Apr        | 2008-Jul        | 4 month         | 1.03                | -0.27               | -0.64        | 0.47         |
| 27    | <b>2010-Oct</b> | <b>2011-Aug</b> | <b>11 month</b> | <b>2.20</b>         | <b>-0.39</b>        | <b>-0.99</b> | <b>0.51</b>  |
| 28    | 2011-Sep        | 2012-May        | 9 month         | 1.51                | -0.26               | -0.73        | 1.34         |
| 29    | 2014-Aug        | 2014-Oct        | 3 month         | 0.71                | -0.09               | 0.22         | 2.10         |
| 30    | 2015-Oct        | 2015-Oct        | 1 month         | 0.50                | 0.18                | 2.37         | 2.51         |

947 TABLE 2. Correlation indices of upper and lower layer temperature and salinity anomalies with modeled  
 948 Indonesian Throughflow (ITF) transport anomalies and observation-based Interdecadal Pacific Oscillation (IPO)  
 949 index and Oceanic Niño Index for *hindcast* (bold), *buoyancy* (italic), *wind* (normal). \* denotes that correlation  
 950 is statistically non-significant ( $p > 0.01$ ). A 12 months rolling mean has been applied to all time series.

|          | Temp 0 – 200m<br>( <b>hindcast</b> , <i>buoyancy</i> , wind) | Sal 0 – 200m<br>( <b>hindcast</b> , <i>buoyancy</i> , wind) | Temp 200 – 600m<br>( <b>hindcast</b> , <i>buoyancy</i> , wind) | Sal 200 – 600m<br>( <b>hindcast</b> , <i>buoyancy</i> , wind) |
|----------|--|---|--|---|
| ITF      | <b>0.38</b> , <i>0.04*</i> , 0.48                            | <b>-0.36</b> , -0.2, -0.38                                  | <b>0.44</b> , -0.03*, 0.46                                     | <b>0.37</b> , <i>0.02*</i> , 0.35                             |
| ITF detr | <b>0.47</b> , <i>0.05*</i> , 0.6                             | <b>-0.44</b> , -0.25, -0.47                                 | <b>0.54</b> , -0.04*, 0.55                                     | <b>0.46</b> , <i>0.02*</i> , 0.43                             |
| IPO      | <b>-0.62</b> , -0.14, -0.74                                  | <b>0.57</b> , <i>0.29</i> , 0.57                            | <b>-0.72</b> , <i>0.09*</i> , -0.68                            | <b>-0.54</b> , <i>0.01*</i> , -0.45                           |
| ONI      | <b>-0.61</b> , -0.16, -0.74                                  | <b>0.5</b> , <i>0.24</i> , 0.55                             | <b>-0.69</b> , <i>0.04*</i> , -0.62                            | <b>-0.53</b> , -0.06*, 0.40                                   |

951 Table A1. Detected Marine Cold Spells using the 10th percentile of the modeled monthly Ningaloo Niño index  
 952 (NNI). The highlighted events agree with years identified as Ningaloo Niña years by Kataoka et al. (2014), who  
 953 based their detection on DJF averages of the NNI.

| Event | Start           | End             | Duration       | Intensity [°C] | Salinity [psu] | ONI         | CWI          |
|-------|-----------------|-----------------|----------------|----------------|----------------|-------------|--------------|
| 1     | 1958-Apr        | 1958-May        | 2 month        | -0.77          | 0.17           | 0.84        | -2.27        |
| 2     | 1958-Jul        | 1958-Aug        | 2 month        | -0.62          | 0.14           | 0.50        | 0.50         |
| 3     | 1960-Jan        | 1960-Jan        | 1 month        | -0.63          | 0.05           | -0.10       | -0.36        |
| 4     | 1960-May        | 1960-Jun        | 2 month        | -0.70          | 0.08           | 0.02        | -0.81        |
| 5     | 1964-Apr        | 1964-Apr        | 1 month        | -0.85          | 0.07           | -0.33       | -0.55        |
| 6     | 1966-Mar        | 1966-Mar        | 1 month        | -0.82          | 0.14           | 0.98        | 0.17         |
| 7     | 1966-Jul        | 1966-Sep        | 3 month        | -0.58          | 0.16           | 0.10        | -0.16        |
| 8     | 1968-Mar        | 1968-Oct        | 8 month        | -1.47          | 0.16           | 0.16        | -0.29        |
| 9     | 1969-Jun        | 1969-Jun        | 1 month        | -0.73          | 0.12           | 0.43        | 1.13         |
| 10    | 1970-May        | 1970-May        | 1 month        | -0.70          | 0.11           | 0.04        | 0.61         |
| 11    | 1971-Dec        | 1971-Dec        | 1 month        | -0.52          | -0.12          | -0.90       | -1.80        |
| 12    | 1977-Mar        | 1977-Apr        | 2 month        | -0.75          | -0.14          | 0.29        | -1.80        |
| 13    | 1985-Jan        | 1985-Jan        | 1 month        | -0.69          | 0.06           | -1.04       | -1.78        |
| 14    | 1986-Aug        | 1986-Aug        | 1 month        | -0.48          | 0.08           | 0.44        | -1.43        |
| 15    | <b>1986-Oct</b> | <b>1987-Feb</b> | <b>5 month</b> | <b>-0.97</b>   | <b>0.10</b>    | <b>1.14</b> | <b>0.02</b>  |
| 16    | 1987-Dec        | 1988-Jan        | 2 month        | -0.87          | 0.14           | 0.96        | -0.25        |
| 17    | 1990-Jul        | 1990-Sep        | 3 month        | -0.73          | 0.10           | 0.37        | 0.08         |
| 18    | <b>1991-Feb</b> | <b>1991-Feb</b> | <b>1 month</b> | <b>-1.08</b>   | <b>0.13</b>    | <b>0.26</b> | <b>-4.63</b> |
| 19    | 1991-Nov        | 1991-Nov        | 1 month        | -0.55          | 0.09           | 1.21        | 0.68         |
| 20    | 1992-Jun        | 1992-Jun        | 1 month        | -0.67          | 0.20           | 0.73        | 0.85         |
| 21    | 1992-Sep        | 1992-Oct        | 2 month        | -0.67          | 0.15           | -0.19       | -1.48        |
| 22    | <b>1993-Feb</b> | <b>1993-Jul</b> | <b>6 month</b> | <b>-1.32</b>   | <b>0.21</b>    | <b>0.51</b> | <b>-1.55</b> |
| 23    | 1993-Oct        | 1993-Nov        | 2 month        | -0.53          | 0.12           | 0.07        | 0.70         |
| 24    | <b>1998-Feb</b> | <b>1998-Feb</b> | <b>1 month</b> | <b>-0.86</b>   | <b>0.13</b>    | <b>1.93</b> | <b>-3.13</b> |
| 25    | 2002-Nov        | 2002-Dec        | 2 month        | -0.93          | 0.20           | 1.23        | -0.63        |
| 26    | 2003-Jul        | 2003-Dec        | 6 month        | -0.66          | 0.19           | 0.26        | -1.29        |
| 27    | 2004-Mar        | 2004-Mar        | 1 month        | -0.67          | 0.15           | 0.23        | -3.51        |
| 28    | <b>2005-Jan</b> | <b>2005-Feb</b> | <b>2 month</b> | <b>-1.04</b>   | <b>0.17</b>    | <b>0.61</b> | <b>-2.07</b> |
| 29    | 2005-Oct        | 2006-Jan        | 4 month        | -0.81          | 0.13           | -0.62       | -1.75        |
| 30    | 2007-Mar        | 2007-Mar        | 1 month        | -0.74          | 0.14           | -0.03       | -2.96        |
| 31    | 2010-Feb        | 2010-Feb        | 1 month        | -0.91          | 0.13           | 1.31        | 0.11         |
| 32    | 2010-Apr        | 2010-Apr        | 1 month        | -0.94          | 0.20           | 0.44        | -2.02        |
| 33    | 2016-May        | 2016-Jun        | 2 month        | -0.93          | 0.26           | 0.24        | -2.76        |
| 34    | 2016-Sep        | 2016-Sep        | 1 month        | -0.79          | 0.18           | -0.68       | -3.72        |

## LIST OF FIGURES

- Fig. 1.** Bathymetric map (model bathymetry) and schematic ocean circulation (after Gordon et al. (2012) and Menezes et al. (2014)) in the region of interest (a) and a snapshot of modeled upper layer temperature in February 2011 (b). The gray isoline in both panels denotes the 1000 m isobath. The Ningaloo Niño box and defined Leeuwin Current band are marked with a legend. Additionally, sections of time-mean modeled temperature (c) and meridional velocity (d) at 24°S are shown. . . . . 49
- Fig. 2.** Mean sea surface height derived from monthly-mean fields between 1993-2015 for *hindcast* (left) and satellite observations (AVISO, right) as gray contours (10 cm intervals) and associated variance in shading (note logarithmic color scale). The 0 cm isoline is marked in black. 50
- Fig. 3.** Leading mode of Empirical Orthogonal Function (EOF) for monthly anomalies of HadISST (a), hindcast SST (b) and hindcast SSS (c). The associated Principal Component (PC) time-series for HadISST and hindcast SST is shown in (d) and for hindcast salinity in (e) together with the respective modeled Ningaloo Niño Index timeseries on the right y-axis. . . . . 51
- Fig. 4.** Time series of surface temperature (a) and salinity (b) anomaly averaged spatially over the Ningaloo Niño box (110 – 117°E, 22 – 32°S). Detected extreme events are marked in color, where red denotes heatwaves and blue cold spells. Monthly NNI timeseries derived from observational datasets for temperature (OISSTv2) and salinity (Argo-ISAS15) are plotted in yellow. All anomalies have been derived with reference to the full length of the respective time series. . . . . 52
- Fig. 5.** Composite vertical profiles in Ningaloo Niño box (110 – 116°E, 22 – 32°S) for marine heatwaves and cold spells for temperature (a), salinity (b) and meridional velocity anomalies (c). Different colors, as marked in legend, denote the hindcast simulation and two sensitivity experiments. Gray shading marks 95% significance interval obtained from the Monte-Carlo simulation. The dashed lines in c) show the composites within the Leeuwin Current band only. . . . . 53
- Fig. 6.** Temperature-salinity diagram for composites of marine heatwaves (left) and cold spells (right) averaged over NNI box over the upper 800 m (top) and individual points within the Leeuwin Current (bottom, see Fig. 1) between 22 – 32°S in *hindcast*. The color shading denotes the temperature anomaly associated with the detected extreme events. The gray isolines represent potential density referenced to the surface. The gray dots represent modeled time-mean water mass properties in the larger eastern Indian Ocean region and the Indonesian archipelago (75 – 150°E, 30 – 40°S) for reference. . . . . 54
- Fig. 7.** Marine heatwave spatial composites for temperature and salinity anomalies at selected depth levels in *hindcast*, *buoyancy* and *wind*. NNI box is marked in black for reference. . . . . 55
- Fig. 8.** Average temperature (top) and salinity (bottom) anomalies in *hindcast* at selected depth levels during the 2010/2011 Ningaloo Niño event (2010/10 - 2011/07). . . . . 56
- Fig. 9.** a) Time series (rolling mean of 30 days) of the meridional wind anomaly and latent heat flux averaged over NNI box from JRA55 forcing fields. b)-j) Monthly vertical profiles of temperature (left column), salinity (middle column) and meridional velocity (right column) anomalies over the course of the 2010/2011 Ningaloo Niño event for *hindcast* (top row), *buoyancy* (middle row), and *wind* (bottom row). . . . . 57

|      |   |    |
|------|---|----|
| 998  | <b>Fig. 10.</b> Monthly spatial surface temperature (top) and salinity (bottom) anomaly evolution during        |    |
| 999  | the 2010/2011 Ningaloo Niño event in <i>hindcast</i> . The Ningaloo Niño Box is marked for                      |    |
| 1000 | reference. . . . .  | 58 |
| 1001 | <b>Fig. 11.</b> Hovmoeller diagram of NNI temperature and salinity anomalies (a,b). Time series of de-          |    |
| 1002 | trended NNI temperature and salinity averaged over the upper 200 m (c,d) and averaged                           |    |
| 1003 | over 200 – 600 m (e,f). On the right y-axis in c-f the Oceanic Niño Index (ONI) is shown in                     |    |
| 1004 | gray. The correlation index $r$ between both time series in each panel is shown in the top left                 |    |
| 1005 | corner (all correlations are significant with $p < 0.01$ ). Note that the ONI y-axis is inverted in             |    |
| 1006 | all panels. . . . .   | 59 |
| 1007 | <b>Fig. 12.</b> Mean modeled vertical profiles of temperature (top), salinity (center) and meridional veloc-    |    |
| 1008 | ity (bottom) anomalies in NNI box for selected events. The maximum value of the coastal                         |    |
| 1009 | wind index (CWI) and the mean Oceanic Niño Index (ONI) during the events are given in                           |    |
| 1010 | the top panels. If an event lasted more than one month, monthly profiles are plotted in gray. . . .             | 60 |
| 1011 | <b>Fig. 13.</b> Summarizing schematic of depth structure associated with a) marine heatwaves (Ningaloo          |    |
| 1012 | Niño) and b) cold spells (Ningaloo Niña) and c) mean vertical profiles in the Ningaloo Niño                     |    |
| 1013 | box. . . . .  | 61 |
| 1014 | <b>Fig. B1.</b> Composite vertical profiles in Leeuwin Current band for marine heatwaves and cold spells        |    |
| 1015 | for temperature (a), salinity (b) and meridional velocity anomalies (c). Different colors, as                   |    |
| 1016 | marked in legend, denote the hindcast simulation and two sensitivity experiments. Gray                          |    |
| 1017 | shading marks 95% significance interval obtained from the Monte-Carlo simulation. The                           |    |
| 1018 | dashed lines in c) show the composites within the Leeuwin Current band only. . . . .                            | 62 |
| 1019 | <b>Fig. B2.</b> Marine cold spell spatial composites for temperature and salinity anomalies at selected depth   |    |
| 1020 | levels in <i>hindcast</i> , <i>buoyancy</i> and <i>wind</i> . NNI box is marked in black for reference. . . . . | 63 |
| 1021 | <b>Fig. B3.</b> Mean seasonal modeled temperature anomalies along 24°S a) and averaged across section           |    |
| 1022 | b). Full monthly temperature profiles averaged across section are shown in c). Red isolines                     |    |
| 1023 | in a) represent potential density referenced to the surface. . . . .  | 64 |

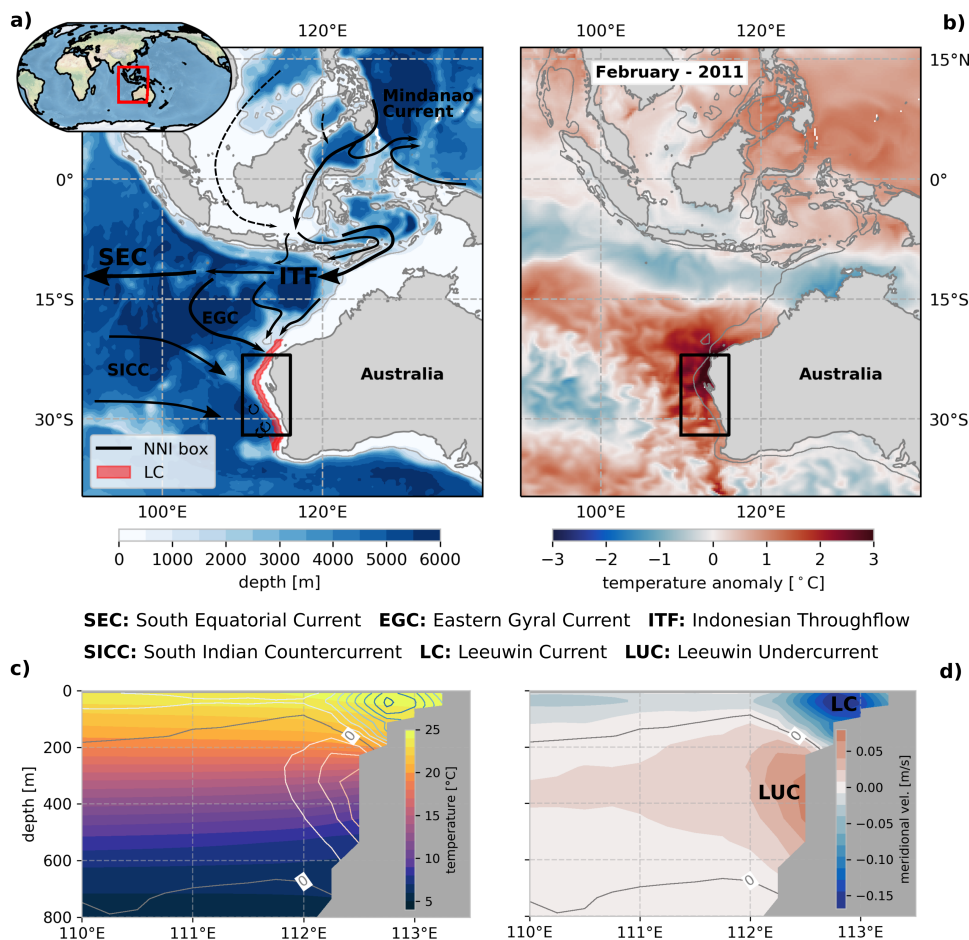


FIG. 1. Bathymetric map (model bathymetry) and schematic ocean circulation (after Gordon et al. (2012) and Menezes et al. (2014)) in the region of interest (a) and a snapshot of modeled upper layer temperature in February 2011 (b). The gray isoline in both panels denotes the 1000m isobath. The Ningaloo Niño box and defined Leeuwin Current band are marked with a legend. Additionally, sections of time-mean modeled temperature (c) and meridional velocity (d) at 24°S are shown.

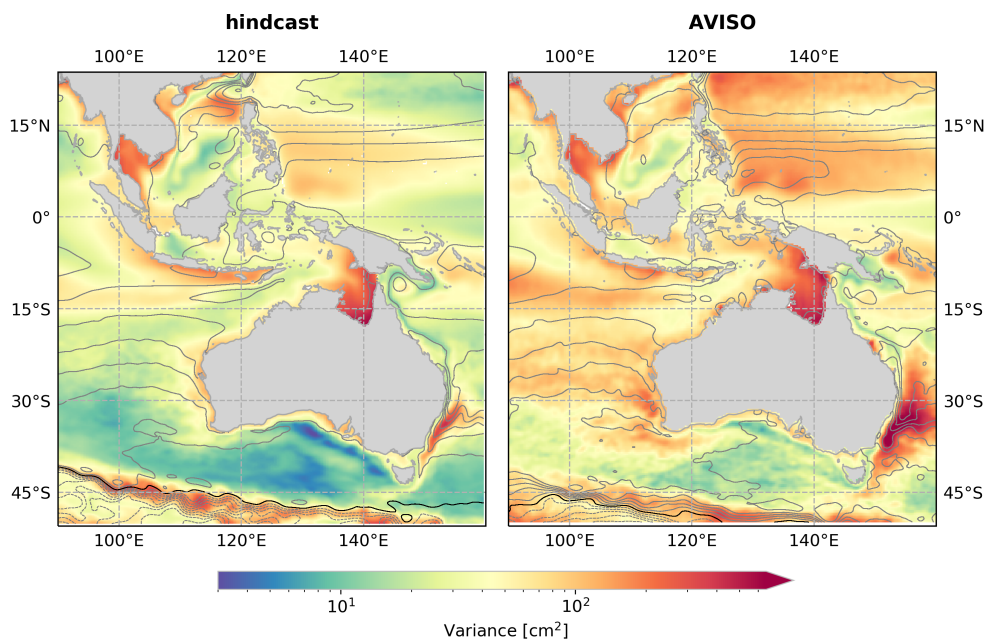


FIG. 2. Mean sea surface height derived from monthly-mean fields between 1993-2015 for *hindcast* (left) and satellite observations (AVISO, right) as gray contours (10cm intervals) and associated variance in shading (note logarithmic color scale). The 0cm isoline is marked in black.

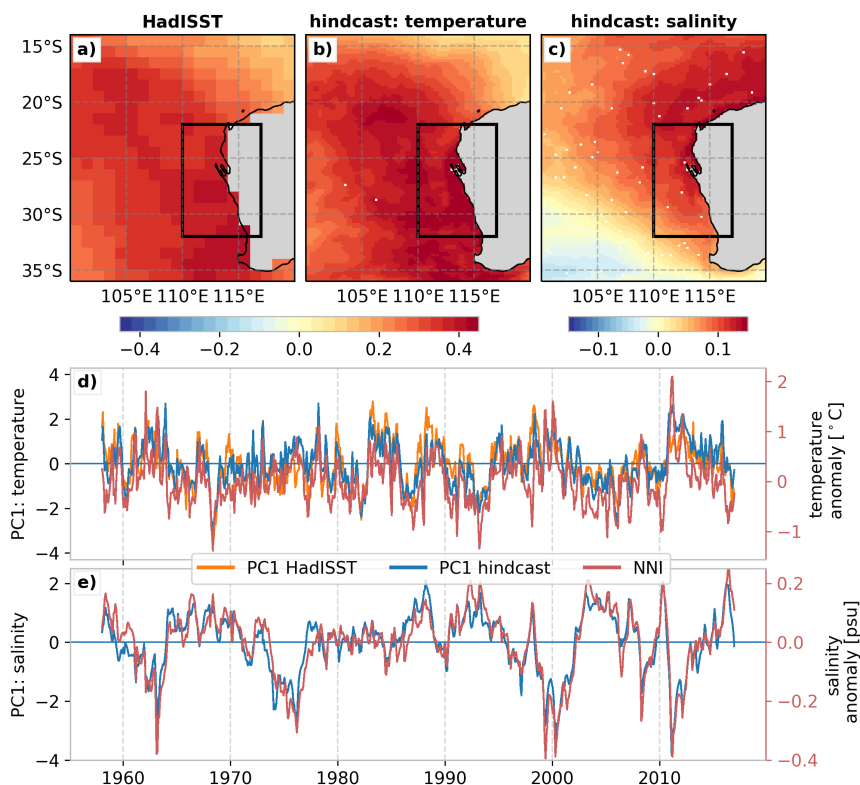


FIG. 3. Leading mode of Empirical Orthogonal Function (EOF) for monthly anomalies of HadISST (a), hindcast SST (b) and hindcast SSS (c). The associated Principal Component (PC) timeseries for HadISST and hindcast SST is shown in (d) and for hindcast salinity in (e) together with the respective modeled Ningaloo Niño Index timeseries on the right y-axis.



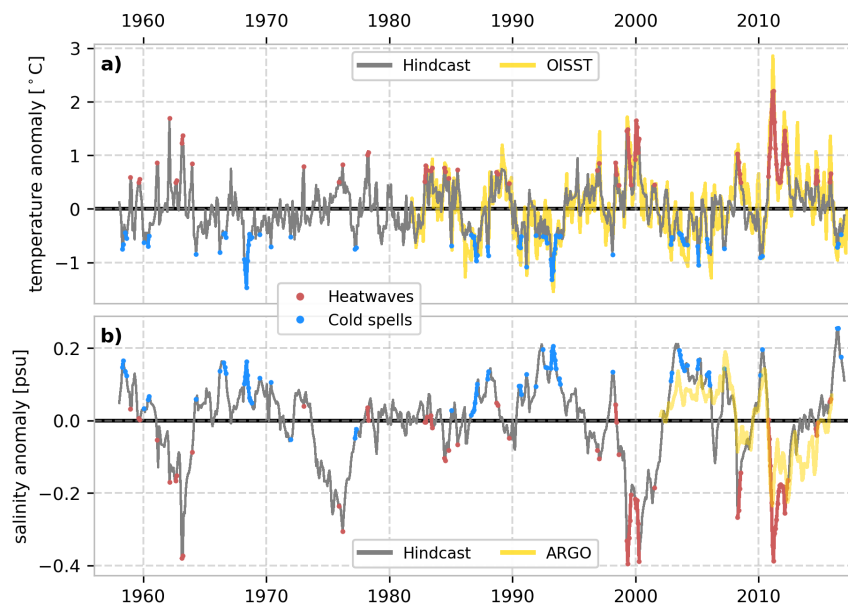


FIG. 4. Time series of surface temperature (a) and salinity (b) anomaly averaged spatially over the Ningaloo Niño box (110 – 117°E, 22 – 32°S). Detected extreme events are marked in color, where red denotes heatwaves and blue cold spells. Monthly NNI timeseries derived from observational datasets for temperature (OISSTv2) and salinity (Argo-ISAS15) are plotted in yellow. All anomalies have been derived with reference to the full length of the respective time series.

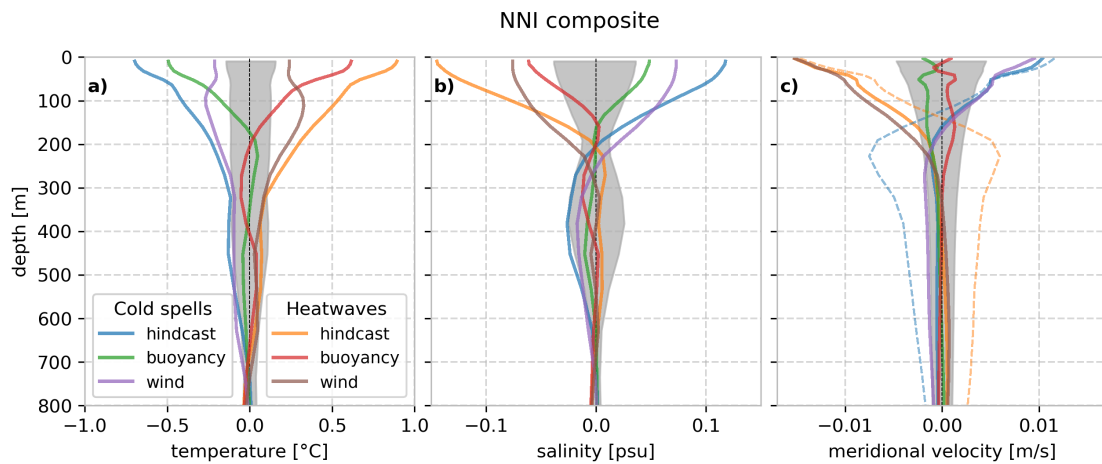


FIG. 5. Composite vertical profiles in Ningaloo Niño box (110 – 116°E, 22 – 32°S) for marine heatwaves and cold spells for temperature (a), salinity (b) and meridional velocity anomalies (c). Different colors, as marked in legend, denote the hindcast simulation and two sensitivity experiments. Gray shading marks 95% significance interval obtained from the Monte-Carlo simulation. The dashed lines in c) show the composites within the Leeuwin Current band only.

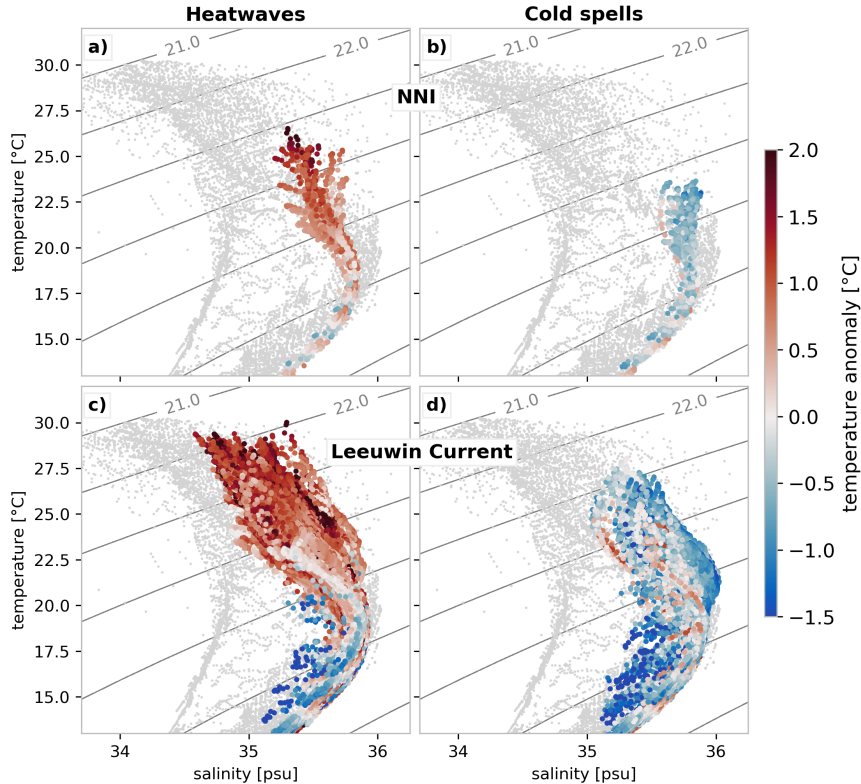


FIG. 6. Temperature-salinity diagram for composites of marine heatwaves (left) and cold spells (right) averaged over NNI box over the upper 800m (top) and individual points within the Leeuwin Current (bottom, see Fig. 1) between 22 – 32°S in *hindcast*. The color shading denotes the temperature anomaly associated with the detected extreme events. The gray isolines represent potential density referenced to the surface. The gray dots represent modeled time-mean water mass properties in the larger eastern Indian Ocean region and the Indonesian archipelago (75 – 150°E, 30 – 40°S) for reference.

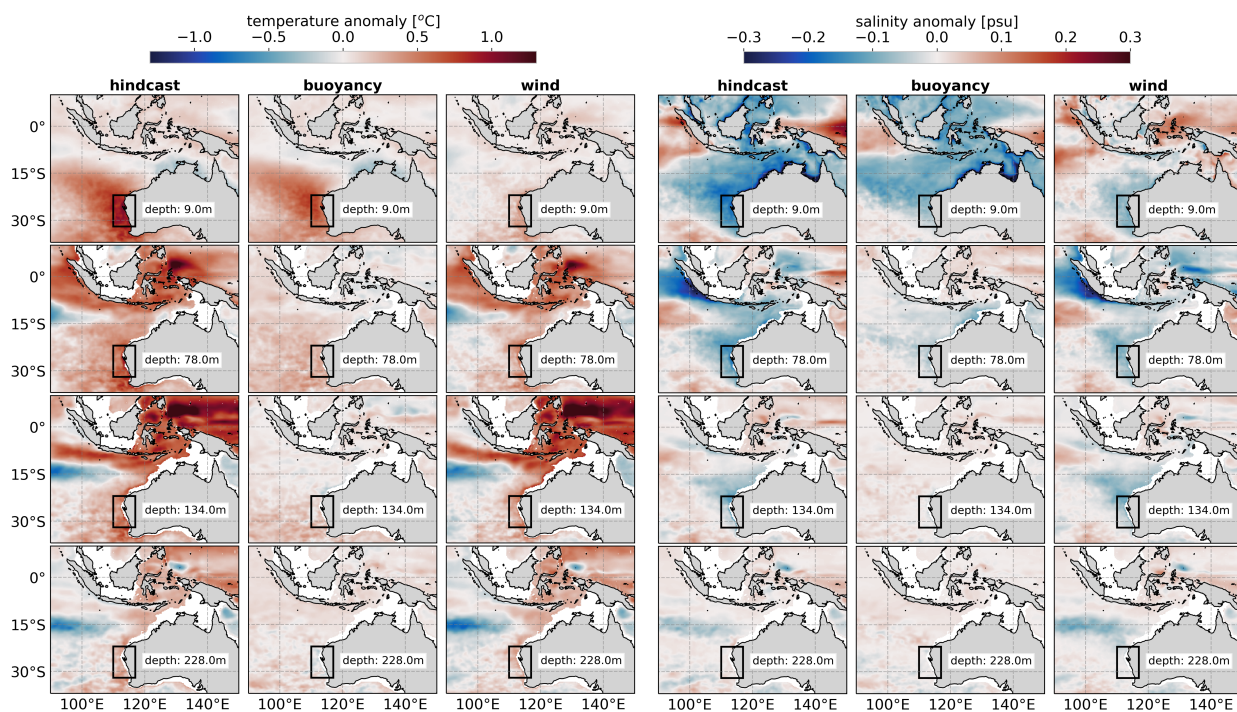


FIG. 7. Marine heatwave spatial composites for temperature and salinity anomalies at selected depth levels in

*hindcast, buoyancy and wind*. NNI box is marked in black for reference.

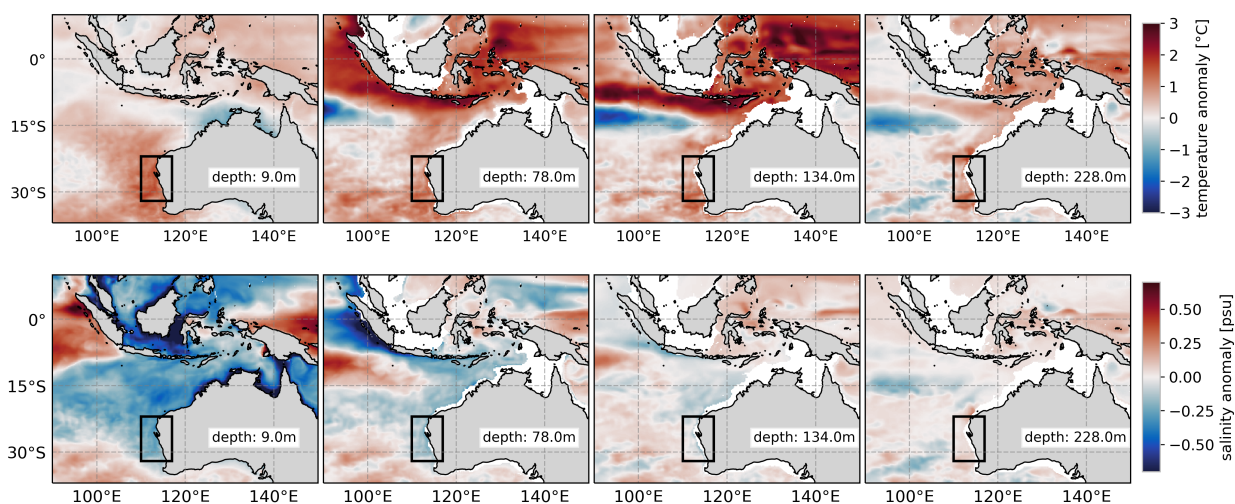


FIG. 8. Average temperature (top) and salinity (bottom) anomalies in *hindcast* at selected depth levels during the 2010/2011 Ningaloo Niño event (2010/10 - 2011/07).

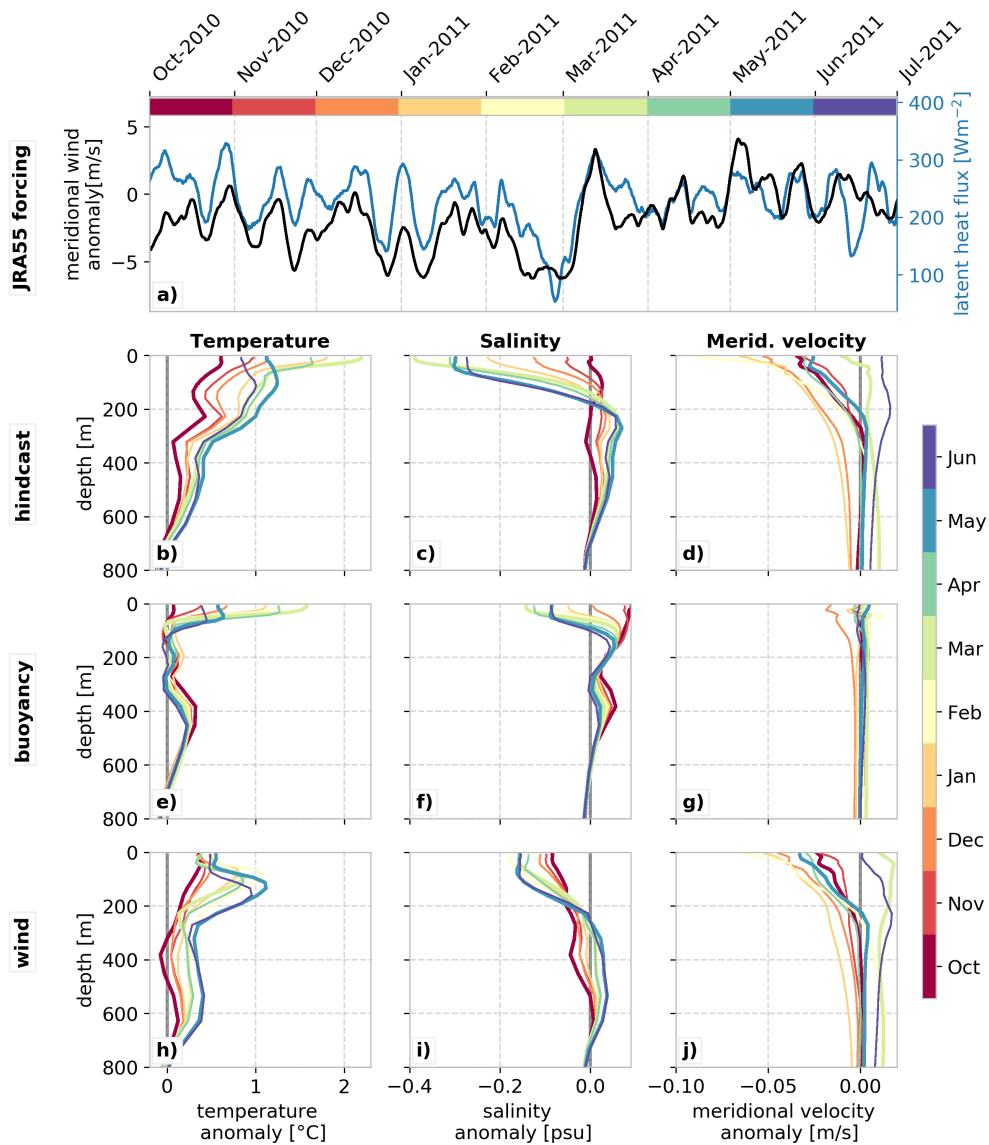


FIG. 9. a) Time series (rolling mean of 30 days) of the meridional wind anomaly and latent heat flux averaged over NNI box from JRA55 forcing fields. b)-j) Monthly vertical profiles of temperature (left column), salinity (middle column) and meridional velocity (right column) anomalies over the course of the 2010/2011 Ningaloo Niño event for *hindcast* (top row), *buoyancy* (middle row), and *wind* (bottom row).



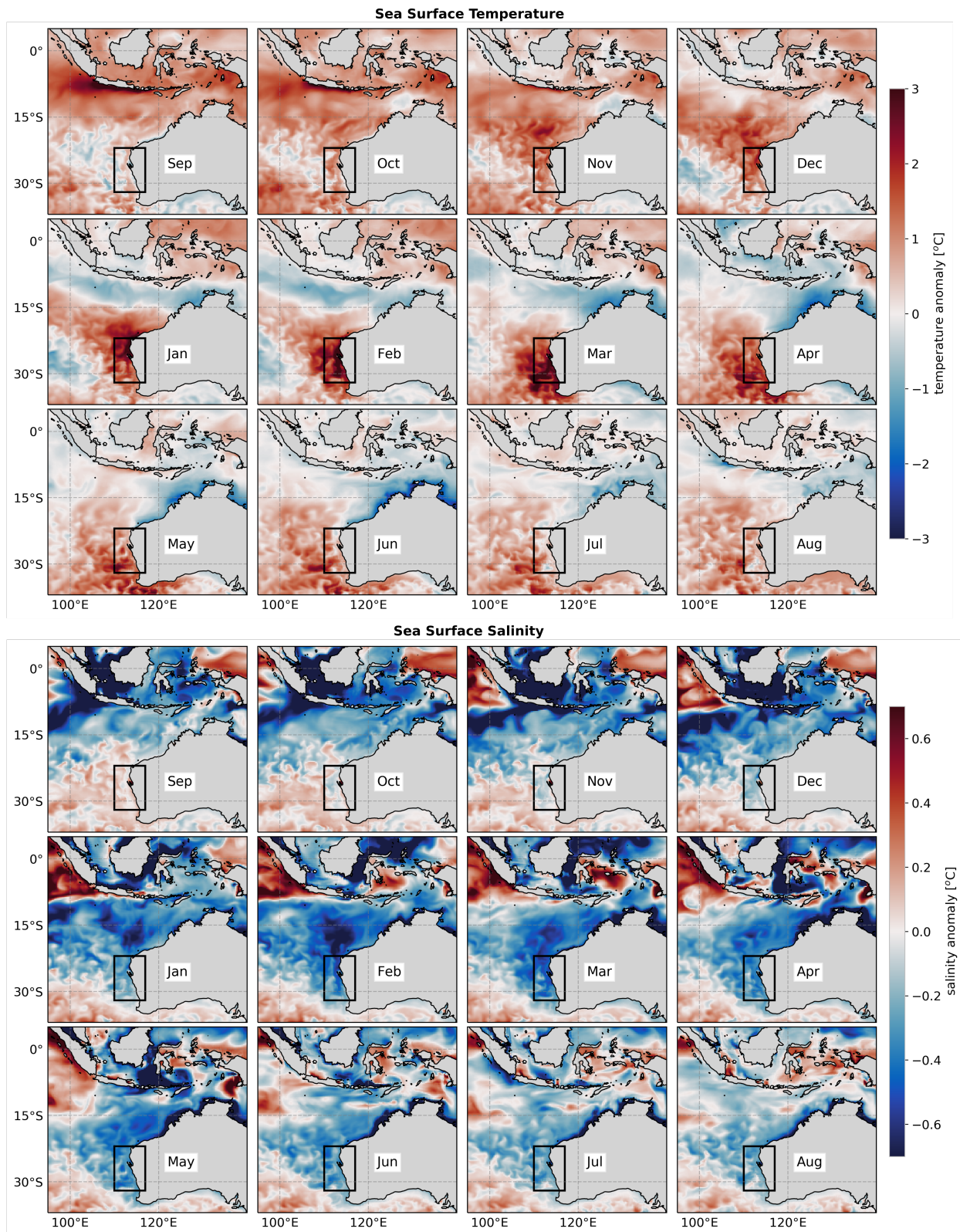


FIG. 10. Monthly spatial surface temperature (top) and salinity (bottom) anomaly evolution during the 2010/2011 Ningaloo Niño event in *hindcast*. The Ningaloo Niño Box is marked for reference.

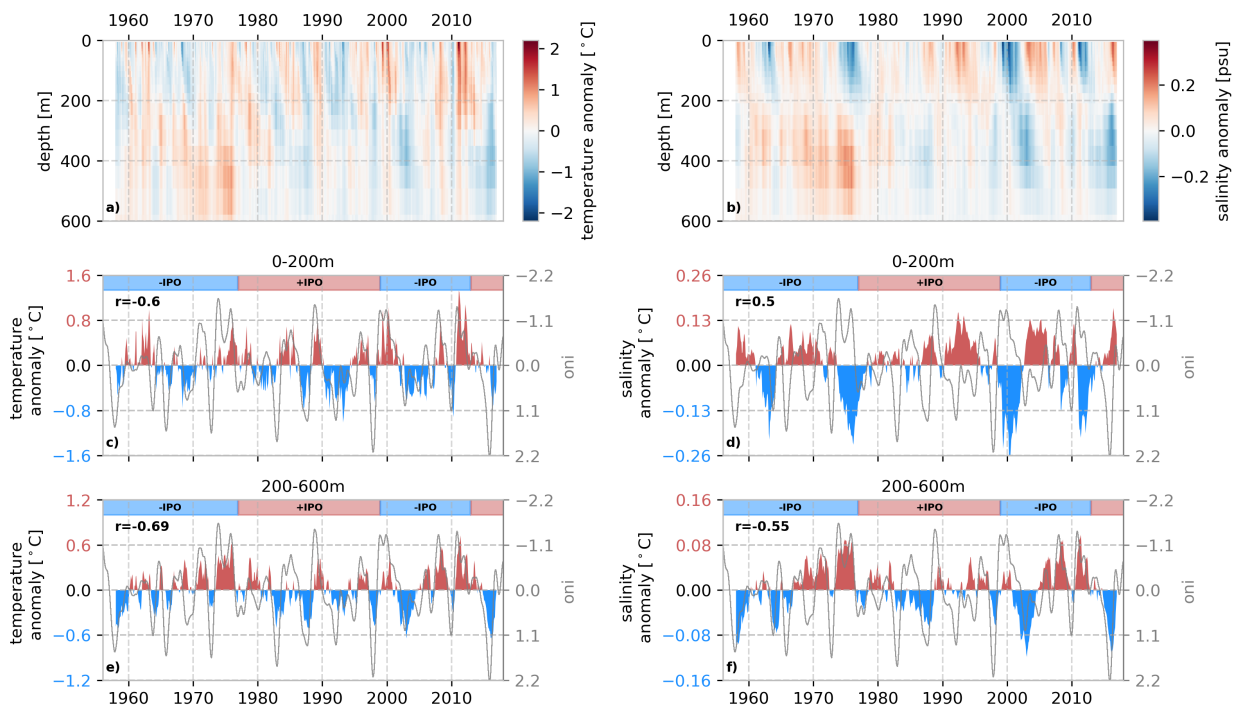


FIG. 11. Hovmoeller diagram of NNI temperature and salinity anomalies (a,b). Time series of detrended NNI temperature and salinity averaged over the upper 200m (c,d) and averaged over 200 – 600m (e,f). On the right y-axis in c-f the Oceanic Nino Index (ONI) is shown in gray. The correlation index  $r$  between both time series in each panel is shown in the top left corner (all correlations are significant with  $p < 0.01$ ). Note that the ONI y-axis is inverted in all panels.



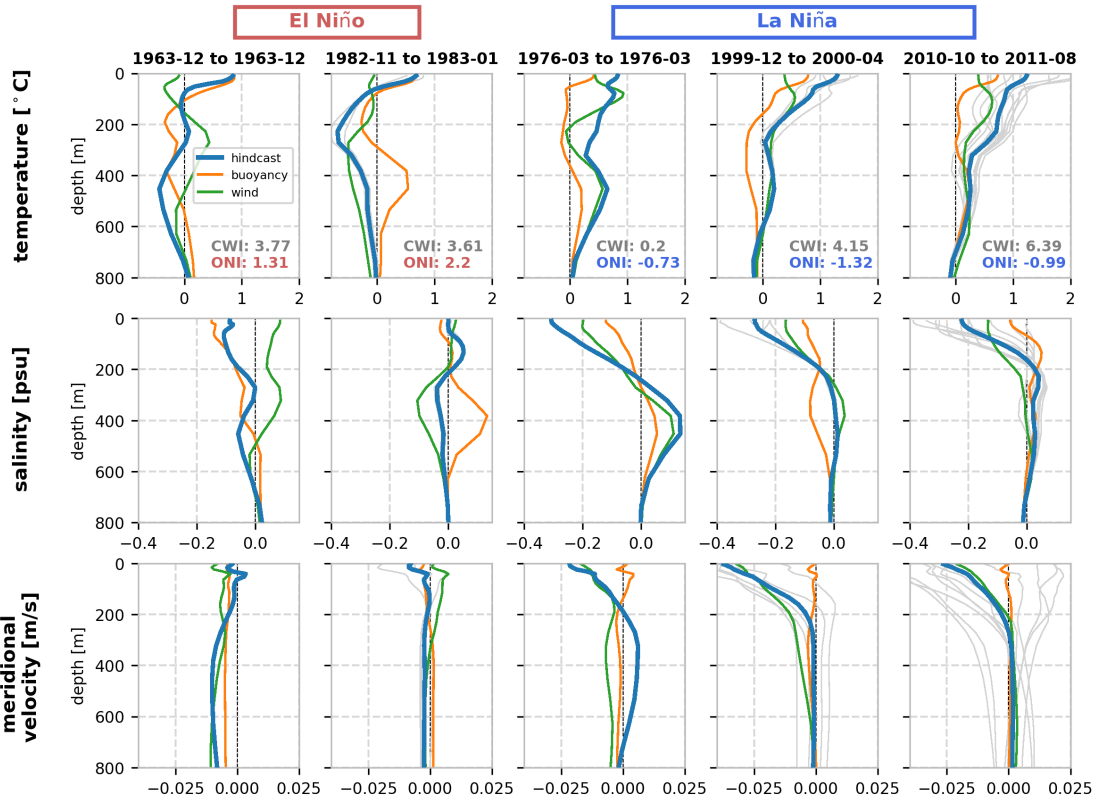


FIG. 12. Mean modeled vertical profiles of temperature (top), salinity (center) and meridional velocity (bottom) anomalies in NNI box for selected events. The maximum value of the coastal wind index (CWI) and the mean Oceanic Niño Index (ONI) during the events are given in the top panels. If an event lasted more than one month, monthly profiles are plotted in gray.

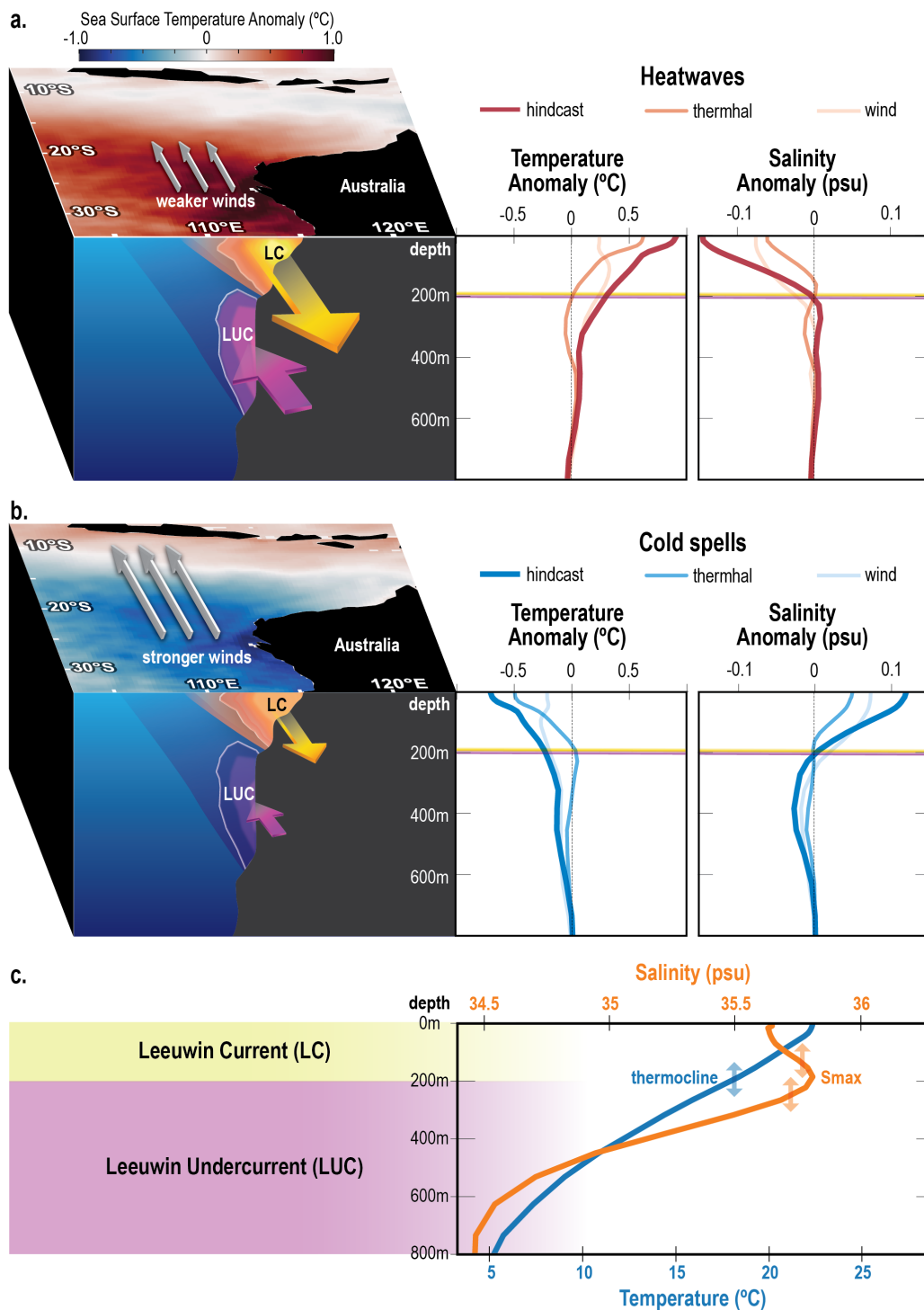


FIG. 13. Summarizing schematic of depth structure associated with a) marine heatwaves (Ningaloo Niño) and b) cold spells (Ningaloo Niña) and c) mean vertical profiles in the Ningaloo Niño box.

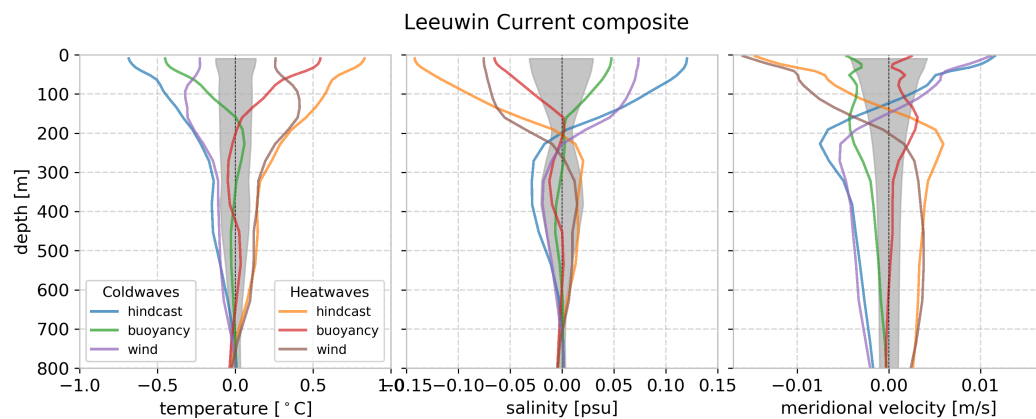


Fig. B1. Composite vertical profiles in Leeuwin Current band for marine heatwaves and cold spells for temperature (a), salinity (b) and meridional velocity anomalies (c). Different colors, as marked in legend, denote the hindcast simulation and two sensitivity experiments. Gray shading marks 95% significance interval obtained from the Monte-Carlo simulation. The dashed lines in c) show the composites within the Leeuwin Current band only.

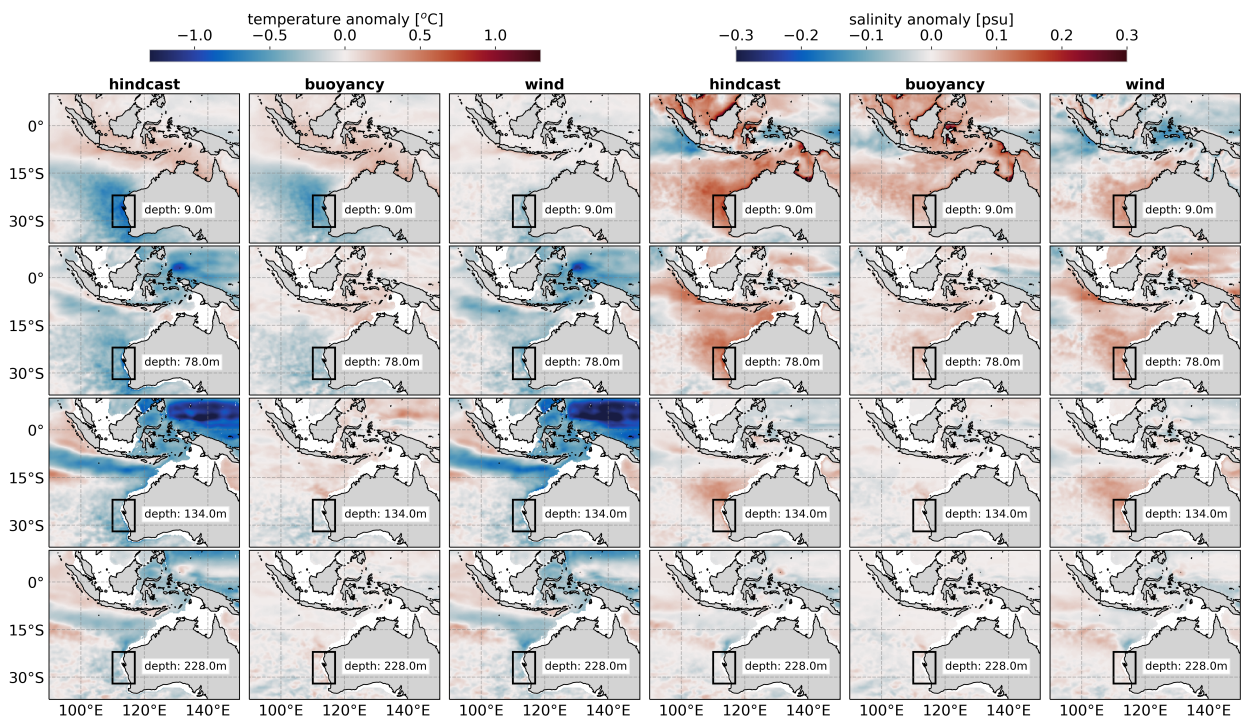


Fig. B2. Marine cold spell spatial composites for temperature and salinity anomalies at selected depth levels in *hindcast*, *buoyancy* and *wind*. NNI box is marked in black for reference.

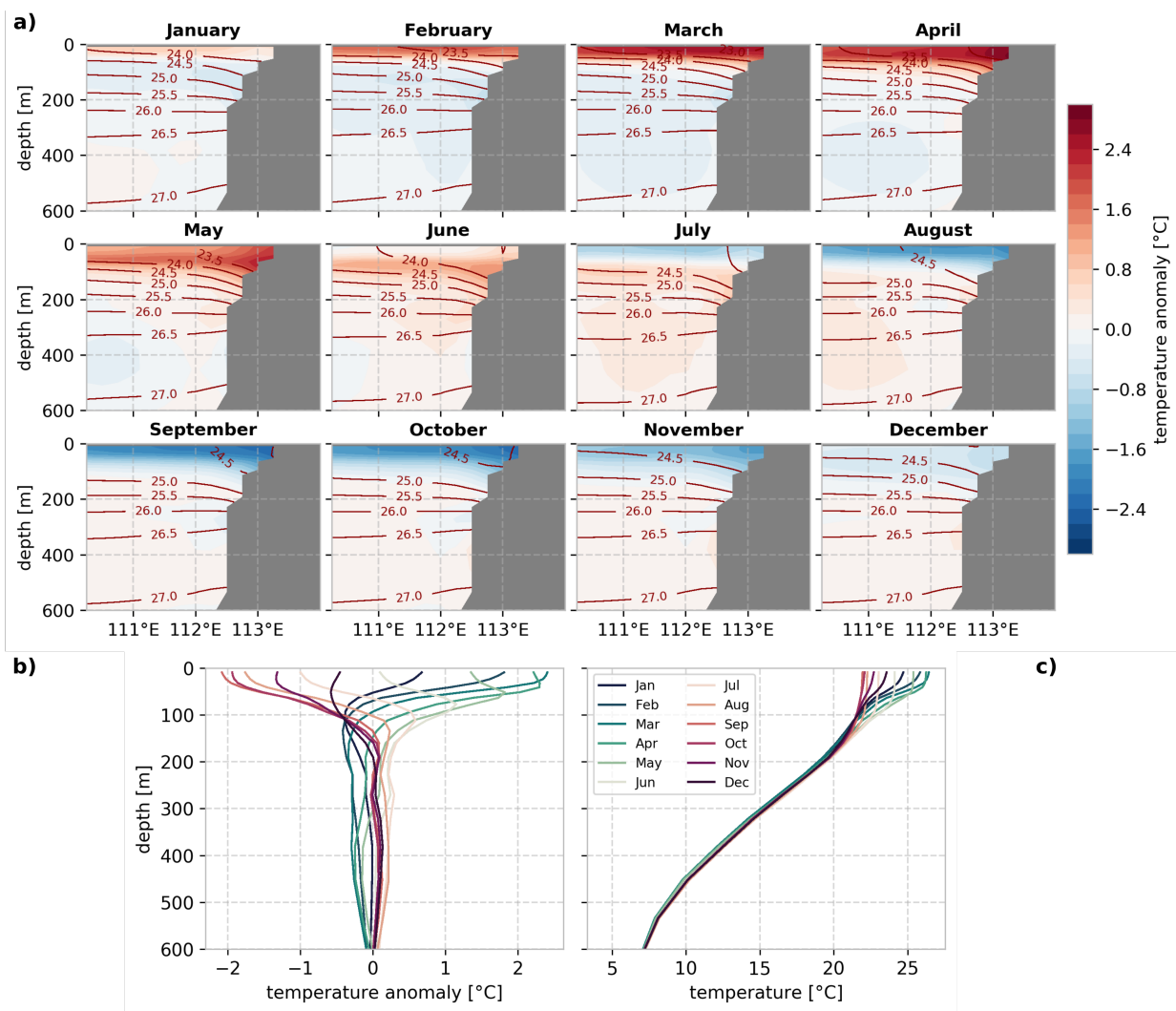


Fig. B3. Mean seasonal modeled temperature anomalies along 24°S a) and averaged across section b). Full monthly temperature profiles averaged across section are shown in c). Red isolines in a) represent potential density referenced to the surface.